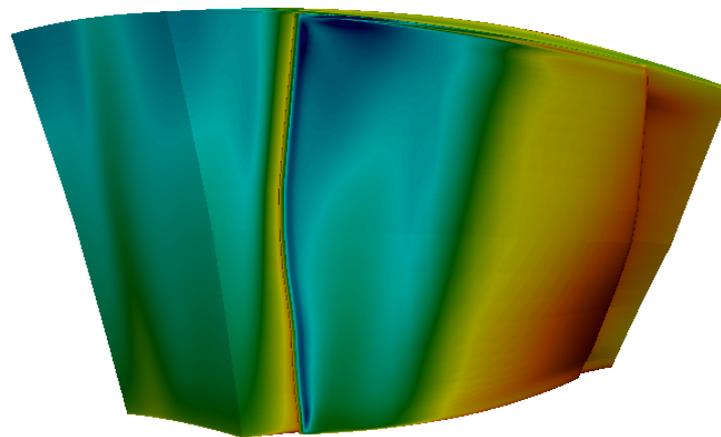




**CHALMERS**  
UNIVERSITY OF TECHNOLOGY

---



# **Reduced order modelling of optimized transonic compressor rotor blades**

Master's thesis in Mechanics and Maritime Sciences

MARCUS RINGSTRÖM  
BJÖRN WALLIN



MASTER'S THESIS 2018:31

# Reduced order modelling of optimized transonic compressor rotor blades

MARCUS RINGSTRÖM  
BJÖRN WALLIN



**CHALMERS**  
UNIVERSITY OF TECHNOLOGY

Department of Mechanics and Maritime Sciences  
*Division of Fluid Dynamics*  
CHALMERS UNIVERSITY OF TECHNOLOGY  
Gothenburg, Sweden 2018

Reduced order modelling of optimized transonic compressor rotor blades  
MARCUS RINGSTRÖM  
BJÖRN WALLIN

© MARCUS RINGSTRÖM, 2018.

© BJÖRN WALLIN, 2018

Supervisor: Gonzalo Montero Villar and Marcus Lejon, Mechanics and Maritime Sciences

Examiner: Tomas Grönstedt, Mechanics and Maritime Sciences

Master's Thesis 2018:31

Department of Mechanics and Maritime Sciences

Division of Fluid Dynamics

Chalmers University of Technology

SE-412 96 Gothenburg

Telephone +46 31 772 1000

Cover: Mach number contour of optimized rotor blade

Typeset in L<sup>A</sup>T<sub>E</sub>X

Printed by Chalmers University of Technology Reproservice

Gothenburg, Sweden 2018

Reduced order modelling of optimized transonic compressor rotor blades  
MARCUS RINGSTRÖM  
BJÖRN WALLIN  
Department of Mechanics and Maritime Sciences  
Chalmers University of Technology

## Abstract

The pursuit of efficient, compact and lightweight aircraft engines are important as it leads to a reduction in specific fuel consumption. Compact and lightweight engines result in compressor designs with high transonic rotor speeds and high stage loading in order to maintain the desired pressure ratio. From an aerodynamic perspective, this poses a challenge since it will be more difficult to design a compressor with respect to high efficiency. Finding a faster design for transonic compressor rotor blades with the same efficiency would therefore be beneficial.

In this thesis the blade generation method, multiple circular arc (MCA) blades represented on conical surfaces was followed to investigate the feasibility of modelling an already optimized 3D compressor rotor blade. In the MCA method conical surfaces are used to approximate the axi-symmetric streamsurfaces in the blade rows, where the MCA method is based on the piecewise preserving of constant turning rate of camber. The complete MCA blade was formed by stacking individual blade elements, where each blade element is defined by 11 design variables. These variables are local blade angles, thickness and axial distances for the critical points on the blade elements; leading edge, trailing edge, maximum thickness and transition. The MCA blade was constructed with 15 spans, resulting in a total of 165 optimizing variables. By employing variable reduction, the total number of optimizing variables was reduced to 75. A multi-variable and multi-objective optimization was made for these 75 variables with the NSGA-II as the optimizer. For the multi-objective optimization two objective functions were formulated to compare the MCA blade with the already optimized 3D blade profile. The objective functions describe the average deviation in the airfoil shape between the blades and the maximum axial cone deviation, which is to ensure that the blade elements are correctly stacked. A design from the Pareto front, which traded the stacking for lower deviation in the blade shape was evaluated using CFD as a performance tool. From the optimization results, it was shown that the shape of the blade elements match the optimized blade well. However, reaching the same stacking of the two blades was not achieved. Results from CFD simulation indicated that the design point is close to the optimized blade with a deviation in polytropic efficiency of 1 %. Combining the optimization with the CFD results it was concluded that the reference blade can be constructed with the MCA model and reach a operating point which was close to the reference, in regards to operating pressure and corrected mass flow.

Keywords: compressor, multiple circular arc, MCA, conical surfaces, optimization, CFD, reduced order modelling, blade design.



# Acknowledgements

First of all we would like to thank Tomas Grönstedt for your support and dedication throughout this thesis. A special thanks to Marcus Lejon and Gonzalo Montero Villar for your extraordinary expertise and help during this project, without your deep knowledge within the field of turbomachinery we would never get this far. We would also like to thank Elias Siggeirsson for the help with the CFD code, which has caused one or two headaches.

Björn Wallin & Marcus Ringström, Gothenburg, May 2018



# Nomenclature

## Abbreviations

CFD	Computational Fluid Dynamics
CFL	Courant-Friedrichs-Lewy
DF	Diffusion Factor
DOF	Degree Of Freedom
DP	Design Point
IGV	Inlet Guide Vane
LE	Leading Edge
MCA	Multiple Circular Arc
NSGA-II	Non-dominated Sorting Genetic Algorithm
PRTT	Total-to-Total Pressure Ratio
RANS	Reynolds-Averaged Navier-Stokes
SNC	Stacked Nurbs Curve
SOR	Surface Of Revolution
TE	Trailing Edge

## Greek Symbols

$\tau_{ij}$	Viscous stress tensor
$\alpha$	Cone half-angle, absolute flow angle
$\delta$	Cirumferential angle coordinate of stacking line, Deviation
$\delta_{ij}$	Kronecker delta
$\epsilon$	Angular coordinate on conic surface as measured from ray passing through blade element leading edge center
$\eta$	Lean angle of stacking line in $r\theta$ -plane (positive in positive $\theta$ -direction)
$\eta_p$	Polytropic efficiency
$\eta_{is}$	Isentropic efficiency
$\gamma$	Specific heat ratio
$\kappa$	Local blade angle, the angle between the local $R$ and the tangent to the local blade element centerline or surface path

---

$\lambda$	Lean angle of stacking line in $rz$ -plane (positive in positive $z$ -direction)
$\mu$	Laminar dynamic viscosity, Sutherland viscosity
$\mu_t$	Turbulent eddy viscosity
$\omega$	Pressure loss coefficient, angular velocity
$\rho$	Density
$\sigma$	Solidity
$\theta$	Circumferential angle coordinate in cylindrical coordinate system (positive $\theta$ -direction is from pressure surface to suction surface, tangential coordinate, camber angle)
$\varepsilon$	Turbulent kinetic dissipation, Deflection
$\xi$	Stagger angle, convenient constant on a segment
$\zeta$	Enthalpy loss coefficient

### Miscellaneous Symbols

'	Isentropic state
–	Ensemble average, Center of area coordinate
~	Favre averaged (density averaged)
"	Unresolved component

### Roman

$A$	Area of blade section
$c$	Rate of turning
$C$	Absolute velocity
$c_\omega$	Swirl velocity
$C_a$	Absolute axial velocity
$C_p$	Static pressure coefficient
$c_p$	Specific heat capacity at constant pressure, Static pressure coefficient
$c_v$	Specific heat capacity at constant volume
$e$	Internal energy
$h$	Enthalpy
$I$	Blade section moment of inertia
$k$	Turbulent kinetic energy
$p$	Static pressure
$Pr$	Laminar Prandtl number
$Pr_t$	Turbulent Prandtl number
$Q$	Heat
$R$	Distance from vertex to point on cone, Gas constant, Radius

---

$r$	Radial coordinate in cylindrical system
$R_s$	Stage pressure ratio
$S$	Entropy
$s$	Path length along blade element centerline or surface, Entropy per unit mass
$S_{ij}$	Strain rate tensor
$T$	Temperature
$t$	Blade thickness
$U$	Blade speed
$u_i$	Velocity vector in cylindrical coordinates
$W$	Work
$x$	Distance from axis of rotation along radial line passing through hub element stacking point
$y$	Coordinate perpendicular to $z$ in constant $x$ -plane
$z$	Axial coordinate from hub element, leading edge center

### Subscripts

0	Total condition
1	Arbitrary reference or known value, inlet rotor
2	Known value, outlet rotor
3	Known value, outlet stator
$c$	Blade centerline
$ca$	Center of area
$h$	Hub element
$i$	Inlet segment or leading edge
$j$	Index denoting axial location
$m$	Maximum thickness point, Meridional coordinate
$max$	Maximum value
$min$	Minimum value
$n$	Normal to blade element centerline
$o$	Outlet segment or trailing edge
$p$	Pressure surface
$s$	Suction surface
$sp$	Stacking point
$t$	Transition point between segments of blade

# Contents

<b>Nomenclature</b>	<b>ix</b>
<b>List of Figures</b>	<b>xv</b>
<b>List of Tables</b>	<b>xvii</b>
<b>1 Introduction</b>	<b>1</b>
1.1 Background . . . . .	1
1.2 Purpose . . . . .	2
1.3 Limitations . . . . .	2
<b>2 Theory</b>	<b>3</b>
2.1 Transonic axial compressor . . . . .	3
2.2 Thermodynamics . . . . .	4
2.2.1 Equation of state . . . . .	4
2.2.2 First law of thermodynamics . . . . .	5
2.2.3 Second law of thermodynamics . . . . .	5
2.2.4 Clausius Gibbs equation . . . . .	6
2.3 Blade Geometry . . . . .	7
2.3.1 Compressor cascade blade nomenclature . . . . .	7
2.3.2 Coordinate system . . . . .	8
2.4 Compressor performance . . . . .	10
2.4.1 Shock structure in multiple circular arc blades . . . . .	10
2.4.2 Efficiency . . . . .	11
2.4.3 Euler Work Equation . . . . .	12
2.4.4 Loss Mechanisms in Axial Compressor Blades . . . . .	13
2.4.5 Performance Characteristics For Transonic Axial Compressors	16
2.5 CFD . . . . .	17
2.5.1 Favre Averaging . . . . .	17
2.5.2 Governing Equations And Turbulence Modeling . . . . .	18
2.5.3 Wall Functions . . . . .	20
<b>3 Methodology</b>	<b>21</b>
3.1 MCA . . . . .	21
3.1.1 MCA Blade Generation Procedure . . . . .	22
3.2 Optimization . . . . .	35
3.2.1 Blade Representation . . . . .	35

3.2.2	Objective Functions . . . . .	36
3.2.3	Multi-objective optimization . . . . .	37
3.2.4	Optimizer . . . . .	37
3.2.5	Variable Range . . . . .	38
3.2.6	Optimization Framework . . . . .	39
3.3	CFD . . . . .	40
3.3.1	Numerical Method . . . . .	40
3.3.2	Computational Domain . . . . .	43
3.3.3	Settings . . . . .	44
<b>4</b>	<b>Results</b>	<b>45</b>
4.1	Optimization . . . . .	45
4.2	CFD . . . . .	47
4.2.1	Stage Performance . . . . .	47
4.2.2	Simulation Results . . . . .	49
<b>5</b>	<b>Conclusion</b>	<b>53</b>
5.1	Future Work . . . . .	54
	<b>Bibliography</b>	<b>55</b>
<b>A</b>	<b>Appendix 1</b>	<b>I</b>



# List of Figures

2.1	<i>Sketch of an axial flow compressor</i>	3
2.2	<i>2D compressor cascade geometry</i>	7
2.3	<i>Coordinate system for an axial compressor</i>	8
2.4	<i>Shock structure of a 2D compressor cascade</i>	10
2.5	<i>Velocity diagram for a single compressor stage</i>	12
2.6	<i>Characteristic map for a transonic axial compressor</i>	16
3.1	<i>Conical surface approximation of axisymmetric streamsurface [2]</i>	21
3.2	<i>Conical coordinate system for blade element layout [2]</i>	22
3.3	<i>Blade element nomenclature [2]</i>	23
3.4	<i>Definition of the blade thickness path [2]</i>	24
3.5	<i>Cylindrical and cartesian coordinate system for the blade [2]</i>	31
3.6	<i>Conical coordinate system with blade element center of area radius illustrated</i>	34
3.7	<i>Reference blade represented by airfoils on conical surfaces</i>	36
3.8	<i>Preliminary camberline used to determine initial range of thickness and axial distance of transition/maximum thickness point</i>	38
3.9	<i>Flowchart of optimization procedure</i>	39
3.10	<i>3D grid surfaces and Blade-to-blade plane for rotor stator configuration</i>	43
4.1	<i>Comparison of MCA and reference blade elements at hub, mid and tip illustrated in <math>r\theta</math> plane for the individual optimization</i>	45
4.2	<i>Pareto front from the final iteration</i>	46
4.3	<i>Selected MCA design and reference blade at hub, mid and tip from the pareto front illustrated in the <math>r\theta</math> plane</i>	46
4.4	<i>Compressor performance of MCA and reference blade at design speed</i>	47
4.5	<i>Cascade comparison of Mach number for the blades at 80% span</i>	49
4.6	<i>Cascade comparison of static pressure for the blades at 80% span</i>	49
4.7	<i>Cascade comparison of static pressure for the blades at 95% span</i>	49
4.8	<i>Comparison of leading edge thickness for the two blade profiles</i>	50
4.9	<i>Normalized radial span distribution of total pressure before and after rotor</i>	51
4.10	<i>Normalized radial span distribution of swirl angle after the rotor and stator</i>	51



# List of Tables

2.1	<i>Values of thermodynamic constants for air assuming a calorically perfect gas . . . . .</i>	5
2.2	<i>Description of geometrical properties for a 2D compressor cascade . . . . .</i>	7
2.3	<i>Description of flow parameters for a 2D compressor cascade . . . . .</i>	8
2.4	<i>Values of closure model constants . . . . .</i>	19
4.1	<i>Performance for optimized and reference blade at design speed . . . . .</i>	48



# 1

## Introduction

### 1.1 Background

In order to reduce the specific fuel consumption, aircraft engines are becoming more compact and lightweight, leading to a reduction in the number of compressor stages. A reduction of compressor stages lead to higher stage loading and also higher blade-tip speeds and hence an increase in Mach number. Higher Mach numbers contribute to a more complex compressor design, increasing computational cost. It would therefore be preferred to find a fast and simple method for generating transonic compressor rotor blades.

A well known blade generation method is the multiple circular arc (MCA) method. It was developed to control shock losses with the ability to control the chordwise turning distribution [2]. In the MCA method the blade surfaces are constructed by two circular arcs, which defines the chordwise turning. By constructing the blade surfaces with circular arcs the chordwise turning is restricted, thus leading to a more constrained design. The constraint in the MCA method is the reason for the method being a simpler design, more constraints equals less parameters to modify. However, the method must be investigated so that the constraint does not alter the possibility of achieving good performance. Since compressor blades are usually designed to turn the flow on meridional streamlines for which the MCA method cannot handle, an approximation has to be done. The blade elements will instead lie on conical surfaces, representing axi-symmetric streamsurfaces.

## 1.2 Purpose

The purpose of the thesis is to recreate an already optimized 3D blade profile with MCA blade geometry and evaluate the difference in performance. The optimizing process is carried out by using a multi-objective genetic algorithm written in the Python programming language. The performance evaluation is done by using computational fluid dynamics (CFD). The aim of this thesis is to investigate if it is possible to recreate an optimized 3D blade profile with a reduced order model.

## 1.3 Limitations

Since it is a 30 ECTS thesis, there is a time constraint, meaning that the project is limited to optimization and performance evaluation of the optimized blade. Results from CFD can be further investigated if more time is spent on the subject. The thesis includes an extensive description of the MCA method in [2]. The optimization was limited to geometrical deviation from an already optimized blade and not an aerodynamic property. The thesis was limited to comparing a single optimized blade and a comparable analysis of aerodynamic performance was carried out to quantify the difference in performance between the two designs. The thesis did not include testing the stability and accuracy of the method on other blades.

# 2

## Theory

### 2.1 Transonic axial compressor

Transonic axial flow compressors can in modern day aviation be found in both commercial high-bypass ratio turbofan engines as well as military turbofans and turbojets. It consists of a series of stages, where each stage is defined as a series of rotor blades followed by a series of stator blades, illustrated in Fig 2.1.

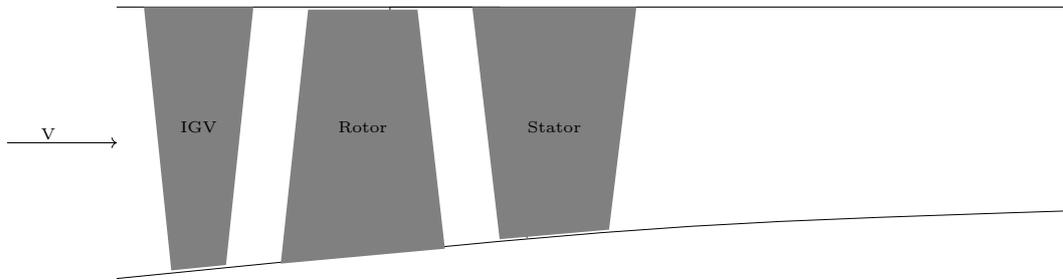


**Figure 2.1:** *Sketch of an axial flow compressor*

The working principle of an axial flow compressor is as follows, the working fluid is initially accelerated by the rotor blades, increasing the kinetic energy of the fluid followed by a fluid deceleration at the stator blades, converting kinetic energy into static pressure. The flow is always moving in a direction subjected to an adverse pressure gradient, making the design of the compressor difficult with increasing pressure ratios. The main task of the internal guide vane, IG V, is to direct the flow into the first compressor stage, permitting the flow angle to vary with rotational speed to improve off-design performance [1]. The IG V pre-swirls the flow to reduce tip Mach number for the first stage. The set of rotor blades are attached to the inner casing, denoted as hub and the stator blades are fixed on the outer casing, denoted as shroud. In transonic compressors, only a part of the outer span and tip is supersonic while the axial velocity is subsonic. In modern transonic compressors, relative Mach numbers up to 1.7 are used and single-stage pressure ratios above 2 are possible [3]. The main advantage of supersonic blade-tip speeds is that very high stage pressure ratios can be obtained due to high work input to the flow [3]. High pressure ratios are important as they make it possible to reduce the number of compressor stages and thus leading to a reduction in engine size and weight. This is important as it allows for a reduction in specific fuel consumption [5].

The performance of compressor blades deteriorates with higher Mach numbers and with Mach numbers exceeding unity in the blade passage, shock waves are generated close to the blade-tip contributing to lower efficiency due to shock losses. High Mach number flows also leads to a reduction in operating range of the compressor because the flow becomes more sensitive to changes in inlet angle [3]. High relative Mach numbers implies high mass flow rates which is favourable as it reduces the flow area, making the machine more compact [3].

## 2.2 Thermodynamics

In this section, the most important parts of thermodynamics, relevant to this thesis are presented.

### 2.2.1 Equation of state

Temperatures and pressures associated with many compressible flow applications assume that the molecular distance between gas particles is widely separated, which implies that the intermolecular forces between the particles are negligible. This is the definition of a perfect gas. For a perfect gas, the equation of state can be written as [4]:

$$p = \rho RT \quad (2.1)$$

where  $\rho$  is the density of air,  $R$  is the specific gas constant,  $T$  is the static temperature and  $p$  is the static pressure.

#### 2.2.1.1 Internal energy and enthalpy

The internal energy can be defined as the sum of rotation, vibration and kinetic energies for all particles in a gas. For a *calorically perfect gas*, i.e, the temperatures and pressures are low enough to consider heat capacity at constant volume and pressure, i.e constant  $c_p$  and  $c_v$ , implying that internal energy,  $e$  and enthalpy,  $h$  can be defined as [4]:

$$\begin{aligned} e &= c_v T \\ h &= c_p T \end{aligned} \quad (2.2)$$

The specific heat capacity at constant pressure and volume can be defined as [4]:

$$c_p = \left( \frac{\partial h}{\partial T} \right)_p \quad (2.3)$$

$$c_v = \left( \frac{\partial e}{\partial T} \right)_v \quad (2.4)$$

For both thermally and calorically perfect gases, following relations can be defined as [4]:

$$R = c_p - c_v \quad (2.5)$$

$$c_p = \frac{\gamma R}{\gamma - 1} \quad (2.6)$$

$$c_v = \frac{R}{\gamma - 1} \quad (2.7)$$

Where  $\gamma$  is defined as  $\gamma = \frac{c_p}{c_v}$ . The values of the constants defined above is listed in table 2.1 below.

$\gamma$	$R$	$c_p$	$c_v$
1.4	$287 \left[ \frac{J}{kgK} \right]$	$1004.5 \left[ \frac{kJ}{kgK} \right]$	$717.5 \left[ \frac{J}{kgK} \right]$

**Table 2.1:** Values of thermodynamic constants for air assuming a calorically perfect gas

## 2.2.2 First law of thermodynamics

The first law of thermodynamics states that, if heat is added and work is done on a system through a complete cycle

$$\oint (dQ - dW) = 0 \quad (2.8)$$

$\oint dQ$  represents heat supplied to the system during the cycle and  $\oint dW$  is the work done by the system. If there is a change in the path between state 1 and state 2, there is a change in energy in the system:

$$E_2 - E_1 = \int_1^2 (dQ - dW) \quad (2.9)$$

where  $E = U + \frac{1}{2}mc^2 + mgz$ . Differential form for an infinitesimal change of state, eq 2.9 can be written as

$$dE = dQ - dW \quad (2.10)$$

Differentiating eq 2.10 with respect to time yields

$$\frac{dE}{dt} = \dot{Q} - \dot{W} \quad (2.11)$$

## 2.2.3 Second law of thermodynamics

The second law of thermodynamics states that, for a system passing through a closed cycle involving exchange of heat can be expressed by the equality [3]:

$$\oint \frac{dQ}{T} \leq 0 \quad (2.12)$$

Where  $dQ$  is an element of heat transferred to the system at a temperature  $T$ . For a reversible process, then  $dQ = dQ_{rev}$ , and the equality in eq 2.12 holds. Reformulating eq 2.12 for a reversible process yields

$$\oint \left( \frac{dQ}{T} \right)_{rev} \leq 0 \quad (2.13)$$

The concept of entropy is an important parameter due to its connection to losses in a thermodynamic system. If there is a change in state between 1 and 2 along a path, then entropy can be defined as [3]:

$$S_2 - S_1 = \int_1^2 \frac{dQ_{rev}}{T} \quad (2.14)$$

for a reversible process

$$S_2 \geq S_1 \quad (2.15)$$

for an adiabatic process,  $dQ = 0$

$$S_2 = S_1 \quad (2.16)$$

For a flow undergoing a process that is both reversible and adiabatic, entropy will be constant, hence no entropy generation in the system. A process that is both reversible and adiabatic is also referred to as *isentropic*.

## 2.2.4 Clausius Gibbs equation

From the first law of thermodynamics, and by using eq 2.14, the differential form of internal energy can be written as [4]:

$$de = Tds - pdv \quad (2.17)$$

$$Tds = de + pdv \quad (2.18)$$

Using the definition of enthalpy

$$h = e + pdv \quad (2.19)$$

Differentiating eq 2.19 yields

$$dh = de + pdv + vdp \quad (2.20)$$

Combining eq 2.18 and 2.20 gives

$$Tds = dh - vdp \quad (2.21)$$

Eq 2.21 is a very important equation as it is written only in terms of system properties. The implication of this equation is that it is valid for a system undergoing any process. Entropy is an important property as it quantifies the amount of work lost in a process, this is of importance when analyzing fluid flows in turbomachinery, as an increase in entropy equates to losses in the system and thus decreasing the efficiency [3].

## 2.3 Blade Geometry

### 2.3.1 Compressor cascade blade nomenclature

A compressor cascade blade is described by a curved camber line and a thickness profile distributed over the camber line [3]. The geometric parameters characterizing the blade is illustrated in Fig 2.2.

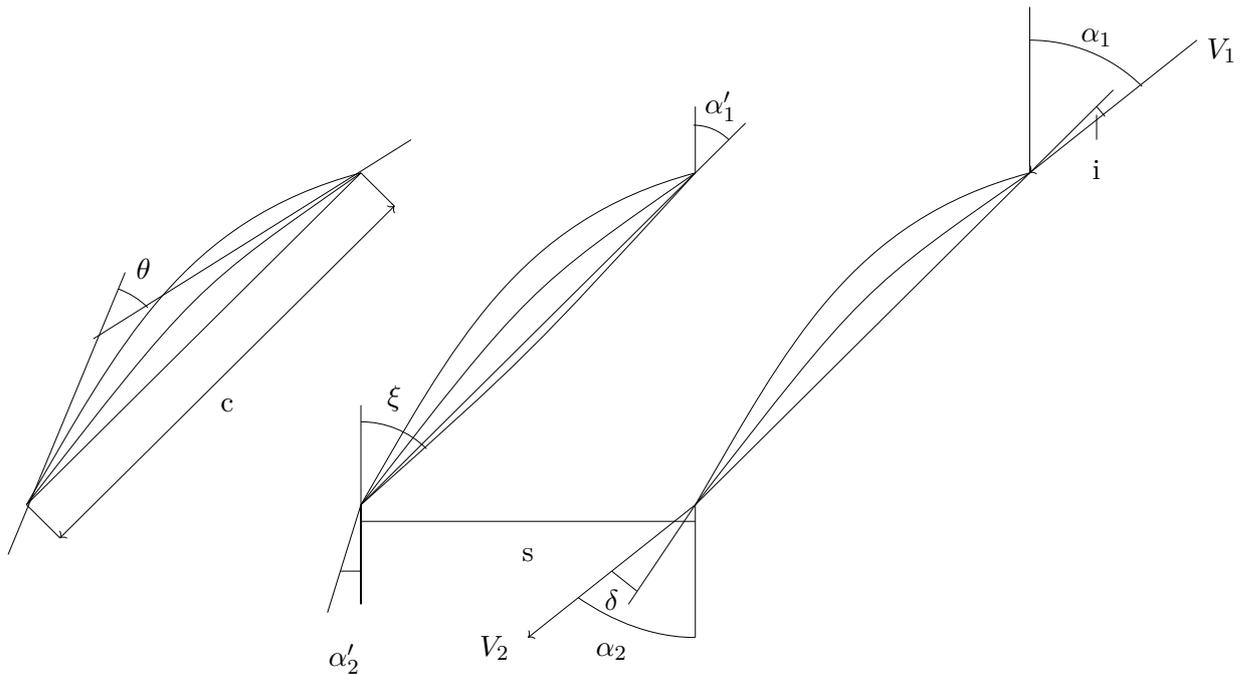


**Figure 2.2:** 2D compressor cascade geometry

The geometrical parameters are defined and briefly described in Table 2.2.

Name	Notation	Description
Stagger angle	$\xi$	Angle between chord line and axial flow direction
Solidity	$\sigma = \frac{c}{s}$	Space and chord ratio
Blade inlet angle	$\alpha_1'$	Angle between camberline and leading edge
Blade outlet angle	$\alpha_2'$	Angle between camberline and trailing edge
Camber angle	$\theta = \alpha_1' - \alpha_2'$	Change in angle of the camberline between le- and te

**Table 2.2:** Description of geometrical properties for a 2D compressor cascade

The flow parameters corresponding to the variables introduced in Table 2.2 above are described in Table 2.3 [3].

Name	Notation	Description
Incidence	$i = \alpha_1 - \alpha'_1$	Difference between inlet flow angle and blade inlet angle
Deflection	$\varepsilon = \alpha_1 - \alpha_2$	Change in angle of the flow
Deviation	$\delta = \alpha_2 - \alpha'_2$	Difference between exit flow angle and blade exit angle

**Table 2.3:** Description of flow parameters for a 2D compressor cascade

### 2.3.2 Coordinate system

In turbomachines it is common to express the geometry in terms of cylindrical coordinates, illustrated in Fig 2.3.

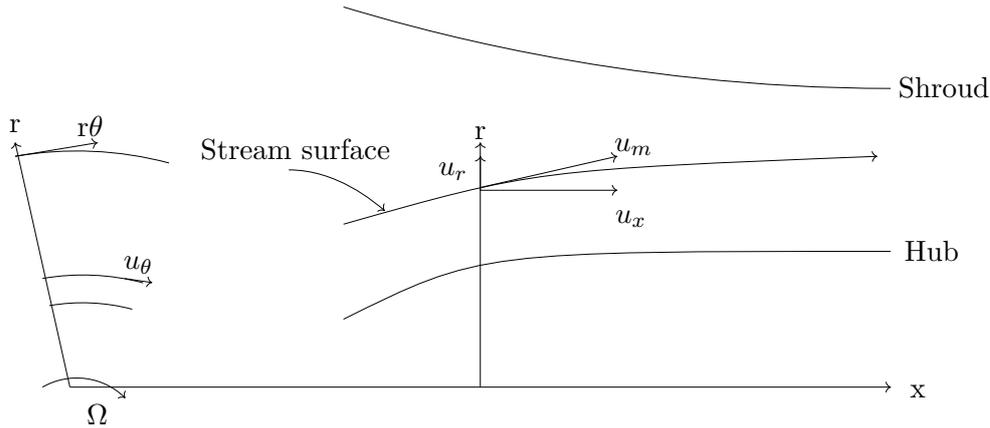


**Figure 2.3:** Coordinate system for an axial compressor

The flow in a compressor is three-dimensional, where all three velocity components varies in all directions. The flow situation is reduced to be axi-symmetric in which the flow moves through the compressor on stream surfaces. The velocity component along a streamsurface is called meridional velocity and is defined as [3]

$$u_m = \sqrt{u_x^2 + u_r^2} \quad (2.22)$$

The total velocity component could be expressed as

$$u = \sqrt{u_x^2 + u_r^2 + u_\theta^2} = \sqrt{u_m^2 + u_\theta^2} \quad (2.23)$$

The swirl angle,  $\alpha$ , is a measure of how much the flow is rotating in the machine and is defined as

$$\alpha = \arctan\left(\frac{u_\theta}{u_m}\right) \quad (2.24)$$

In compressors, the flow field within the rotating blades are described in a frame of reference that is stationary relative to the rotating blades [3]. The relative velocity is found by subtracting the tangential velocity component from the blade speed

$$v_{\theta} = u_{\theta} - U \quad (2.25)$$

The relative flow angle is defined as the angle between the relative flow direction and the meridional direction

$$\beta = \arctan\left(\frac{v_{\theta}}{u_m}\right) \quad (2.26)$$

The relation between the relative and absolute flow angle can be found by combining eq 2.25 and 2.26 [3]:

$$\tan \beta = \tan \alpha - \frac{U}{u_m} \quad (2.27)$$

## 2.4 Compressor performance

### 2.4.1 Shock structure in multiple circular arc blades

Multiple circular arc blades have widely been used to control shock losses and throat area for transonic compressors. For supersonic flows where shock losses in blade passages are prevalent, MCA blades has an advantage due to its ability to control chordwise turning distribution [2]. For supersonic velocities, the flow exhibits a shock pattern similar to Fig 2.4. A detached shock, or bow shock is formed caused by the thickness of the leading edge and by the expansion waves formed by the curvature at the suction surface. The expansion waves interact with the shocks upstream and the strength of the shocks become weaker further upstream. Because of the axi-symmetric geometry, the pattern is repeated and each blade will therefore experience the same shock pattern. Most of the pressure rise is produced by the passage shock formed at the blade leading edge travelling downstream where it terminates in a normal shock somewhere on the neighbouring blade suction surface [6], illustrated in Fig 2.4.

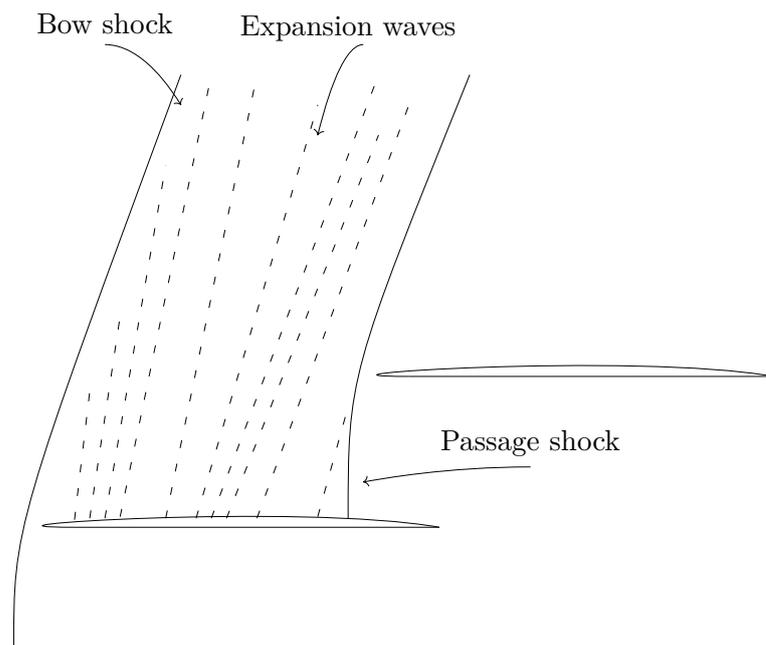


**Figure 2.4:** *Shock structure of a 2D compressor cascade*

The total pressure loss produced by the passage shock relates to the shock strength and consequently the Mach number downstream from the leading edge. When the flow expands through the expansion waves, the flow accelerates, increasing the Mach number. The Mach number after the expansion could be found by using the Prandtl-Meyer function which relates the Mach number before and after the expansion with the flow turning angle. By using MCA blades, the Mach number is reduced by limiting the chordwise turning at the suction surface, leading to a reduction in shock strength and hence total pressure loss [2].

## 2.4.2 Efficiency

In this section, only the most important types of efficiencies will be discussed, isentropic and polytropic efficiency, as they are the most frequently used when dealing with flows in turbomachinery applications.

### 2.4.2.1 Isentropic efficiency

A compressor can be idealized as being adiabatic and reversible, meaning that the entropy gradient is zero. The efficiency of a compressor can be expressed as the ratio between actual and ideal work transfer. Due to the adiabatic nature of compressors, the ideal thermodynamic process is isentropic, hence isentropic efficiency. For a perfect gas, the isentropic efficiency can be written as [1]:

$$\eta_{is} = \frac{\Delta T'_0}{\Delta T_0} = \frac{T'_{02} - T_{01}}{T_{02} - T_{01}} \quad (2.28)$$

where ' denotes the isentropic state. For a perfect gas, the temperature ratio could be expressed in terms of pressure ratio

$$\frac{T'_{02}}{T_{01}} = \left( \frac{p_{02}}{p_{01}} \right)^{\left( \frac{\gamma}{\gamma-1} \right)} \quad (2.29)$$

Combining eq 2.28 and 2.29 yields

$$\eta_{is} = \frac{(p_{02}/p_{01})^{\left( \frac{\gamma-1}{\gamma} \right)} - 1}{(T_{02}/T_{01}) - 1} \quad (2.30)$$

### 2.4.2.2 Polytropic efficiency

By looking at eq 2.30, the isentropic efficiency drops with increasing overall pressure ratio, which could lead to confusion. This can be avoided by using another definition of efficiency for adiabatic compressors, the so-called polytropic efficiency, or small-stage efficiency,  $\eta_p$ . For a real compression, the increase in enthalpy is larger than the ideal enthalpy rise, which can be written as [6]:

$$dh_0 = \frac{1}{\eta_p} dh'_0 = \frac{1}{\eta_p} \frac{dp_0}{p_0} \quad (2.31)$$

By assuming a perfect gas and constant  $\eta_p$  over a finite pressure change, the temperature ratio can be written in terms of pressure ratio

$$\frac{T_{02}}{T_{01}} = \left( \frac{p_{02}}{p_{01}} \right)^{\frac{(\gamma-1)}{\eta_p \gamma}} \quad (2.32)$$

From (2.32),  $\eta_p$  could be rewritten as [6]:

$$\eta_p = \frac{\gamma - 1}{\gamma} \frac{\ln(p_{02}/p_{01})}{\ln(T_{02}/T_{01})} \quad (2.33)$$

If each stage in a multi-stage compressor had the same value of  $\eta_p$ , the polytropic efficiency for the whole compressor would be equal to that stage. Using polytropic efficiency instead of isentropic efficiency may therefore be better to use when analyzing different compressors.

### 2.4.3 Euler Work Equation

For a compressor with angular velocity  $\omega$ , the rate of which the rotor exert work on the fluid is given by the expression

$$\dot{W}_c = \tau\omega = \dot{m}(U_2c_{\omega 2} - U_1c_{\omega 1}) \quad (2.34)$$

Where  $\tau$  is the angular momentum of the fluid passing through the rotor. By assuming that the axial velocity and flow radius is constant, eq 2.34 can be rewritten as

$$\dot{W}_c = \dot{m}U(c_{\omega 2} - c_{\omega 1}) \rightarrow \frac{\dot{W}_c}{\dot{m}} = \Delta W_c = U(c_{\omega 2} - c_{\omega 1}) \quad (2.35)$$

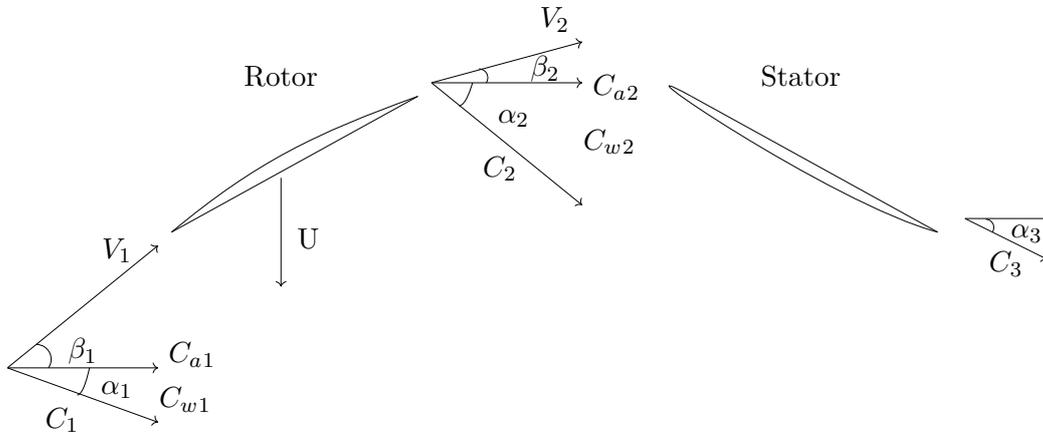


**Figure 2.5:** Velocity diagram for a single compressor stage

The relation for the angles for the rotor and stator can be found from Fig 2.5

$$U = c_{\omega 1} + V_{\omega 1} = C_a \tan \alpha_1 + C_a \tan \beta_1 \quad (2.36)$$

$$U = c_{\omega 2} + V_{\omega 2} = C_a \tan \alpha_2 + C_a \tan \beta_2 \quad (2.37)$$

Combing eq 2.36 and 2.37 yields

$$\tan \alpha_1 + \tan \beta_1 = \tan \alpha_2 + \tan \beta_2 \rightarrow \tan \alpha_2 - \tan \alpha_1 = \tan \beta_1 - \tan \beta_2 \quad (2.38)$$

The result from eq 2.38 and 2.35 give the following relation

$$\Delta W_c = UC_a (\tan \beta_1 - \tan \beta_2) \quad (2.39)$$

This input of energy will be used to raise the pressure of the fluid. This energy will manifest itself as a rise in stagnation temperature of the fluid. The rise in stagnation temperature for a stage can be expressed as [1]

$$\Delta T_{0s} = T_{03} - T_{01} = T_{02} - T_{01} = \frac{UC_a}{c_p} (\tan \beta_1 - \tan \beta_2) \quad (2.40)$$

The rise in pressure is very much dependent on the efficiency of the compression process, the isentropic stage efficiency can be expressed as [1]:

$$\eta_s = \frac{(T_{03}' - T_{01})}{(T_{03} - T_{01})} \quad (2.41)$$

The stage pressure ratio can then be expressed as

$$R_s = \frac{p_{03}}{p_{01}} = \left[ 1 + \frac{\eta_s \Delta T_{0s}}{T_{01}} \right]^{\frac{\gamma}{(\gamma-1)}} \quad (2.42)$$

## 2.4.4 Loss Mechanisms in Axial Compressor Blades

Boundary layer growth and separation on a blade surface has a detrimental impact on efficiency of the compressor. From thermodynamic principles we know that a drop in total pressure lead to a rise in entropy, or lost work, which equate to losses in a thermodynamic system. The task of quantify loss characteristics of separation and boundary layer growth have been proved to be difficult due to a large number of factors involved, including inlet Mach number, surface velocity distribution, Reynolds number and turbulence in the free-stream [3]. Analysis of cascade data have led to the development of correlation models that could predict blade losses and fluid deviation. In this section, these losses will briefly be discussed together with typical loss coefficients in axial compressor blades relevant for this thesis.

### 2.4.4.1 Loss sources

Loss sources in a compressor blade can be defined as [20]:

- Profile losses
- Shock losses
- Tip-leakage losses
- End-wall losses
- Secondary flow losses

#### Profile losses

Profile loss can be divided into blade primary loss and trailing edge mixing loss. Blade primary loss are associated with a loss in total pressure due to viscous forces slowing the fluid down within the boundary layer at the blade surface. Trailing edge mixing loss stem from thickness of the trailing edge and boundary layer thickness on the pressure and suction surface, causing wake defect, mixing and thus entropy generation. Mixing losses can be described as exchange of momentum and energy between the wake and the freestream [15].

#### Shock losses

Shock losses are of concern only for transonic and supersonic compressor rotors. Shocks are highly irreversible and contribute to losses indirectly through boundary layer interaction, leading to boundary layer growth by a rise in static pressure produced by the shock. Entropy generation is thus a unique function of static pressure.

The rise in static pressure lead to boundary layer separation and hence a drop in total pressure [14].

### **Tip-leakage losses**

Arise from flow leaking over the rotor tip and hub clearance of stator blade [14]. The loss mechanism is driven by pressure difference between the pressure and suction surface, causing the flow to roll along the suction surface to form a tip vortex [16]. Cornelius [17] conclude that for sufficiently small tip clearance, the main source of losses are viscous losses generated at the shroud. For larger tip clearance, tip leakage flow increases and the main source of losses are due to mixing [17].

### **Secondary flow losses**

The loss mechanism from secondary flows are similar to those of tip-leakage. Vortex formation results in mixing and dissipation of energy which results in entropy generation and hence losses [20]. In addition, interaction of secondary flow with the wall, boundary layer and wake contribute to additional losses. The source loss mechanism is due to viscous effects, dissipation and mixing [20].

### **End-wall losses**

End-wall loss is also referred to as secondary loss, arise from secondary flows generated at the annulus boundary layers passing through a blade row [14]. The growth of end-wall boundary layer and mixing, together with dissipative effects result in additional losses. End-wall losses, including secondary flow losses and tip-leakage losses contribute to 50-70% of total losses [20].

### 2.4.4.2 Loss coefficients in axial compressors

Modelling losses in compressors are vital as it is directly related to the efficiency of the turbomachine. Loss coefficients, expressed in non-dimensional form are commonly used to quantify losses connected to compressors. Loss coefficients are convenient to use as they are easy to calculate from cascade data. In this section, the most commonly used loss coefficients related to axial compressors are discussed and defined.

#### Total pressure loss coefficient

Total pressure loss coefficient can be defined as an overall measure of the aerodynamic losses through the blade row. For compressors, the total pressure loss coefficient can be defined as [3]:

$$\omega_p = \frac{(p_{01} - p_{02})}{(p_{01} - p_1)} \quad (2.43)$$

Where  $p_{01}$  is the inlet total pressure,  $p_{02}$  is the outlet total pressure and  $p_1$  is the inlet static pressure.

#### Enthalpy loss coefficient

A more useful loss coefficient adopted for design purposes is the enthalpy loss coefficient,  $\zeta$ , which is defined as [14]:

$$\zeta = \frac{h_2 - h_{2s}}{h_{01} - h_1} \quad (2.44)$$

Where  $h_{2s}$  is the final isentropic enthalpy, obtained in an isentropic expansion or compression to the same state as the final static pressure.

#### Static pressure coefficient

One of the main objectives of a compressor is to produce a rise in static pressure, as well as a deflection angle,  $\varepsilon$ . A performance parameter for static pressure is therefore introduced. This parameter is called static pressure coefficient. For compressible flows, the static pressure coefficient can be defined as [3]:

$$C_p = \frac{(p_2 - p_1)}{p_{01} - p_1} \quad (2.45)$$

### 2.4.5 Performance Characteristics For Transonic Axial Compressors

For a transonic axial flow compressor, the performance can graphically be illustrated by a compressor map, shown in Fig 2.6.

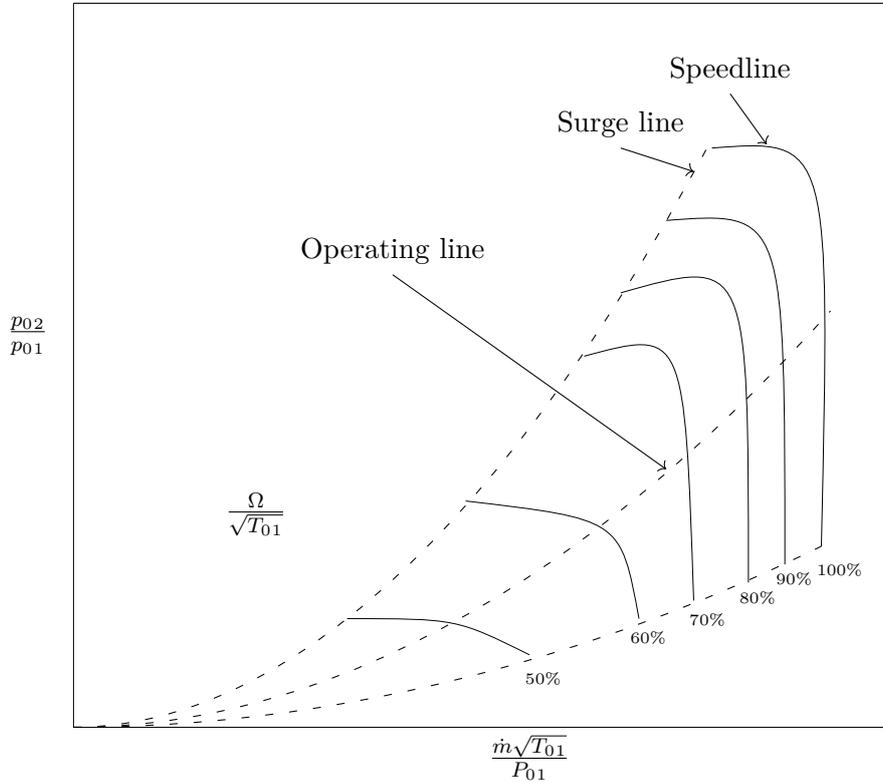


**Figure 2.6:** *Characteristic map for a transonic axial compressor*

Total pressure ratio is plotted as a function of the corrected mass flow,  $\frac{\dot{m}\sqrt{T_{01}}}{P_{01}}$  in the form of curves for fixed values of the corrected rotational speed,  $\frac{\Omega}{\sqrt{T_{01}}}$ , these set of curves is also known as speedlines. Each speedline on the compressor map terminates at a line of instability, also called surge line. The maximum point of the speedline is referred to as surge point. Beyond this point the operation is unstable [3]. Compressor instability can be divided into stall and surge. Compressor stall could be understood as flow separation from the blade's suction- and pressure surface due to large positive or negative angle of attack, the compressor blade is unable to build up enough pressure and the flow starts to break up, leading to flow instabilities. A stalled flow moves in the opposite direction of the blade rotation, giving the name rotating stall [12]. In contrast to stall, compressor surge occurs when the compressor blade is unable to withstand the rise in back pressure, leading to large amplitude oscillations of the flow, which may result in a violent flow reversal out from the compressor, leading to a complete breakdown of the compressor. By looking at the speedlines it can be seen that when the corrected mass flow is at it's maximum the total pressure ratio is at it's minimum. A further decrease in pressure ratio will result in an increase in velocity to a point when it reach sonic conditions at the

throat ( $M=1$ ), the flow is then said to be choked. At this point, a further increase in  $\frac{\dot{m}\sqrt{T_{01}}}{p_{01}}$  is not possible [3]. The point where the flow is choked is also referred to as choke point.

## 2.5 CFD

Computational fluid dynamics has become an indispensable tool in design and analysis of turbomachinery. In this section, the governing equations and the corresponding closure models required to model turbulence are presented and discussed.

### 2.5.1 Favre Averaging

Favre averaging is a filtering method commonly used when dealing with compressible flows as it allows for the transport equations to be written in a form similar to the conventional unfiltered equations. Filtering over an arbitrary flow variable  $\psi$  reads

$$\psi = \tilde{\psi} + \psi'' \quad (2.46)$$

Where  $\tilde{\psi}$  is the Favre filtered quantity and  $\psi''$  is the unresolved component of  $\psi$ . Favre-filtering part of  $\psi$  yields

$$\tilde{\psi} = \frac{\overline{\rho\psi}}{\bar{\rho}} \quad (2.47)$$

Where  $\overline{\rho\psi}$  denotes Reynolds decomposition averaging. Recall that the average of a fluctuating component is zero

$$\overline{\rho\psi''} = 0 \quad (2.48)$$

And

$$\overline{\rho\tilde{\psi}} = \bar{\rho}\tilde{\psi} = \overline{\rho\psi} \quad (2.49)$$

The Favre-filtered equations of momentum, energy and continuity is obtained by applying the Favre filtering operator given by eq 2.47.

## 2.5.2 Governing Equations And Turbulence Modeling

The compressible flow solver used to solve the flow field is based on the compressible RANS equations with realizable  $k$ - $\varepsilon$  as a turbulence model. The choice of turbulence model is based on trade off between computational cost and accuracy. The reason why the realizable  $k$ - $\varepsilon$  is chosen is due to its ability to handle flows with boundary layers subjected to adverse pressure gradients, separation and circulation [9]. The boundary layer is modelled with conventional wall functions. The Favre-filtered Navier-Stokes equations can in compact form be expressed as [7]:

$$\frac{\partial \mathcal{Q}}{\partial t} + \frac{\partial \mathcal{F}_j}{\partial x_j} = \mathcal{H} \quad (2.50)$$

The state vector,  $\mathcal{Q}$ , can be expressed as

$$\mathcal{Q} = \begin{bmatrix} \bar{\rho} \\ \bar{\rho} \tilde{u}_i \\ \bar{\rho} \tilde{e}_0 \\ \bar{\rho} \tilde{k} \\ \bar{\rho} \tilde{\varepsilon} \end{bmatrix} \quad (2.51)$$

The flux vector,  $\mathcal{F}_j$ , can be expressed as

$$\mathcal{F}_j = \begin{bmatrix} \bar{\rho} \tilde{u}_i \\ \bar{\rho} \tilde{u}_i \tilde{u}_j + \bar{p} \delta_{ij} - \tau_{ij} \\ \bar{\rho} \tilde{e}_0 \tilde{u}_j + \bar{p} \tilde{u}_j - c_p \left( \frac{\mu}{Pr} + \frac{\mu_t}{Pr_t} \right) \frac{\partial \tilde{T}}{\partial x_j} - \tilde{u}_i \tau_{ij} \\ \bar{\rho} \tilde{k} \tilde{u}_j - \left( \mu + \frac{\mu_t}{\sigma_k} \right) \frac{\partial \tilde{k}}{\partial x_j} \\ \bar{\rho} \tilde{\varepsilon} \tilde{u}_j - \left( \mu + \frac{\mu_t}{\sigma_\varepsilon} \right) \frac{\partial \tilde{\varepsilon}}{\partial x_j} \end{bmatrix} \quad (2.52)$$

The dissipation and production term from  $k$  and  $\varepsilon$ -equations is included in the source vector  $\mathcal{H}$ , and is given by

$$\mathcal{H} = \begin{bmatrix} 0 \\ 0 \\ 0 \\ P_k - \bar{\rho} \tilde{\varepsilon} \\ (C_{\varepsilon 1} P_k - C_{\varepsilon 2} \bar{\rho} \tilde{\varepsilon}) \frac{\tilde{\varepsilon}}{k} \end{bmatrix} \quad (2.53)$$

The production term,  $P_k$ , is modelled as

$$P_k = \left( \mu_t \left( 2\tilde{S}_{ij} - \frac{2}{3} \frac{\partial \tilde{u}_k}{\partial x_k} \delta_{ij} \right) - \frac{2}{3} \bar{\rho} \tilde{k} \delta_{ij} \right) \frac{\partial \tilde{u}_i}{\partial x_j} \quad (2.54)$$

Where  $\delta_{ij}$  is the kronecker delta,  $(\bar{\rho})$ ,  $(\bar{p})$  represents the average of density and pressure. Velocity vector ( $\tilde{u}_i$ ), total internal energy ( $\tilde{e}_0$ ), temperature ( $\tilde{T}$ ), turbulent kinetic energy ( $\tilde{k}$ ) and turbulence dissipation ( $\tilde{\varepsilon}$ ) represents the Favre-averaged quantities. Reynolds stresses are modeled with the Boussinesq assumption, meaning that Reynolds stresses can be written in terms of turbulent viscosity and mean velocity gradients [8]:

$$-\rho \overline{u_i u_j} = \mu_t \frac{\partial \overline{U}_i}{\partial x_j} \quad (2.55)$$

The viscous stress tensor  $\tau_{ij}$  can for a Newtonian fluid be written as

$$\tau_{ij} = (\mu + \mu_t) \left( 2\tilde{S}_{ij} - \frac{2}{3} \frac{\partial \tilde{u}_k}{\partial x_k} \delta_{ij} \right) - \frac{2}{3} \bar{\rho} \tilde{k} \delta_{ij} \quad (2.56)$$

The strain rate tensor  $\tilde{S}_{ij}$  is defined as

$$\tilde{S}_{ij} = \frac{1}{2} \left( \frac{\partial \tilde{u}_i}{\partial x_j} + \frac{\partial \tilde{u}_j}{\partial x_i} \right) \quad (2.57)$$

The realizable  $k - \varepsilon$  equation include a realizability constraint for the turbulent viscosity  $\mu_t$  [7].

$$\mu_t = \min \left( C_\mu \bar{\rho} \frac{\tilde{k}^2}{\tilde{\varepsilon}}, \frac{0.4 \bar{\rho} \tilde{k}}{\sqrt{\tilde{S}_{ij} \tilde{S}_{ij}}} \right) \quad (2.58)$$

In order to close the system of equations, it is assumed that the gas is thermally perfect, in other words, internal energy, enthalpy and specific heat at constant volume and pressure are described as being functions of temperature only

$$e = e(\tilde{T}) \quad (2.59)$$

$$h = h(\tilde{T}) \quad (2.60)$$

$$c_v = \frac{de}{d\tilde{T}} \quad (2.61)$$

$$c_p = \frac{dh}{d\tilde{T}} \quad (2.62)$$

Values of the closure model constants are listed in table 2.1

$C_\mu$	$C_{\varepsilon 1}$	$C_{\varepsilon 2}$	$\sigma_\varepsilon$	$\sigma_k$
0.09	1.44	1.92	1.3	1

**Table 2.4:** *Values of closure model constants*

### 2.5.3 Wall Functions

The idea of employing wall functions is to apply boundary conditions some distance away from the wall so that strong gradients of the flow variables are not solved close to the wall, saving computational cost to the expense of not resolving the flow in the viscous sub-layer. The first node should be placed in the fully turbulent sublayer ( $30 < y^+ < 100$ ), also called log-law region, where wall functions are valid [9]. In order to use wall functions, modifications of the turbulence models needs to be carried out in order to account for the viscosity-affected near-wall region. In the log-law region, the turbulent shear stress  $-\rho\overline{u_i u_j}$  is equal to the wall shear stress,  $\tau_w$ . Applying Boussinesq assumption yields [8]:

$$\tau_w = -\rho\overline{u_i u_j} = \mu_t \frac{\partial \overline{U}_i}{\partial x_j} \quad (2.63)$$

Using the definition of the wall shear stress,  $\tau_w = \rho u_*^2$ , where  $u_*$  is the friction velocity, the mean velocity  $\overline{U}_i$  can be expressed as [9]:

$$\overline{U}_i = \frac{\tau_w y}{\rho \nu} = \frac{u_*^2 y}{\nu} \quad (2.64)$$

or written in dimensionless form:

$$\overline{U}_i^+ = \frac{y u_*}{\nu} = y^+ \quad (2.65)$$

where  $y^+$  is the dimensionless distance from the wall to the first node. The log-law in dimensionless form reads

$$\overline{U}_i^+ = \frac{1}{\kappa} \ln(y^+) + 5 \quad (2.66)$$

Where  $\kappa$  is the Von Kármán constant. Boundary conditions for the turbulent quantities,  $k$  and  $\varepsilon$  is found by assuming that the flow is in local equilibrium, i.e production equals dissipation. This assumption is valid in the log-law region for  $y^+ > 30$ . The boundary condition for turbulent kinetic energy,  $k$ , is given by [9]

$$k = \frac{u_*^2}{\sqrt{C_\mu}} \quad (2.67)$$

By considering local equilibrium, boundary condition for dissipation is given by [9]:

$$\varepsilon = P_k = \overline{u_i u_j} \frac{\partial \overline{U}_i}{\partial x_j} = u_*^2 \frac{u_*}{\kappa y} = \frac{u_*^3}{\kappa y} \quad (2.68)$$

Where  $\kappa y$  is Prandtl's mixing length.

# 3

## Methodology

In this chapter the methodology for the MCA blade generation, adopted from [2], is described together with the optimization of blade parameters and CFD configuration.

### 3.1 MCA

The conical approximation of the streamsurfaces used in the blade generation is seen in Fig 3.1 where  $\alpha$  is the cone half-angle.

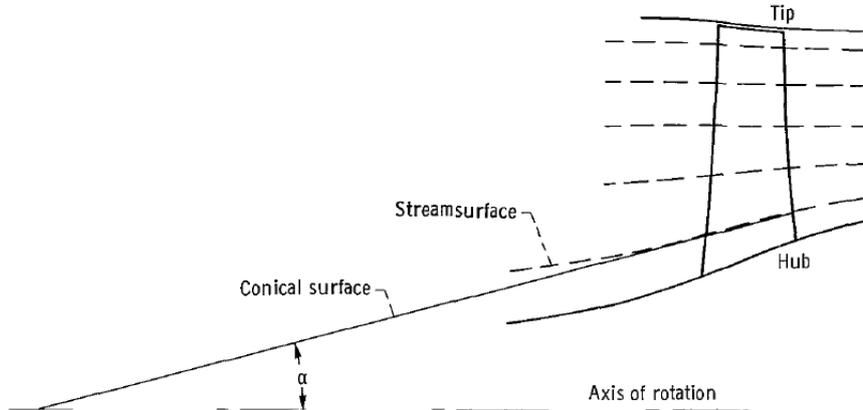


**Figure 3.1:** *Conical surface approximation of axisymmetric streamsurface [2]*

An illustration of the blade layout on a cone is shown in Fig 3.2, where the  $R\epsilon$  coordinate system is used. In this coordinate system the cone surface is unwrapped on a plane and the blade elements can with ease be described in a plane instead. In the  $R\epsilon$  coordinate system  $R$  is the length of an ray from the cone vertex to an arbitrary point in the circle sector and  $\epsilon$  is the angle from an reference ray to a ray through the arbitrary point. The conical approximation of the streamsurface is defined by  $r_i$ ,  $r_o$  and  $z$ . They are radius for the leading edge center, trailing edge center and the axial distance between the two radii which then forms the conical surface by revolution around the rotation axis. The blade angle  $\kappa$  is defined by the angle between a ray,  $R$ , and the tangent of the blade surface or centerline.

The methodology followed in [2] is only for the layout of blade elements on conical

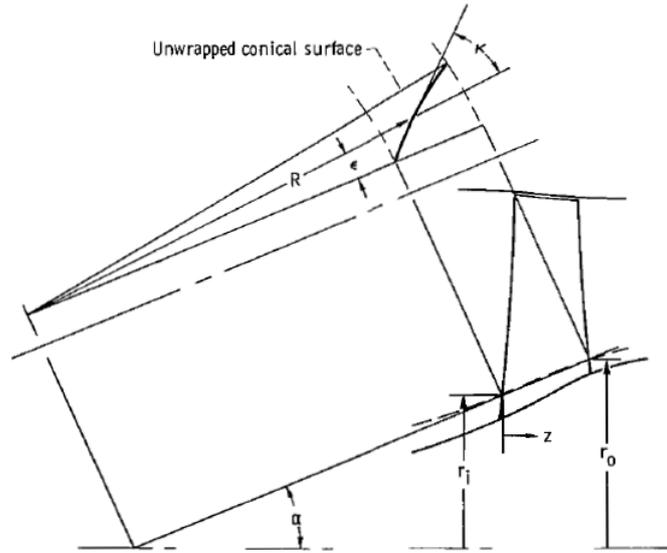


**Figure 3.2:** *Conical coordinate system for blade element layout [2]*

surfaces and omits the prior steps in the design process needed to establish the blade properties. Each blade element is specified by 11 parameters:

- Radius from axis of rotation to the leading edge center,  $r_{ic}$
- Radius from axis of rotation to the trailing edge center,  $r_{oc}$
- Thickness at the leading edge,  $t_i$
- Thickness at the maximum thickness point,  $t_m$
- Thickness at the trailing edge,  $t_o$
- Blade angle between R ray and centerline tangent at the leading edge,  $\kappa_{ic}$
- Blade angle between R ray and centerline tangent at the transition point,  $\kappa_{tc}$
- Blade angle between R ray and centerline tangent at the trailing edge,  $\kappa_{oc}$
- Axial distance from leading edge center to the centerline maximum thickness point,  $z_{mc}$
- Axial distance from the leading edge center to the centerline transition point,  $z_{tc}$
- Axial distance from the leading edge center to the trailing edge center,  $z_{oc}$

For the layout procedure, the blade element surfaces and centerline are constructed by two segments, inlet and outlet, with their own constant turning rate,  $d\kappa/ds$ . Where the inlet and outlet segment becomes tangent is called the transition point. The parameters required before the layout and some nomenclature are illustrated in Fig 3.3 and 3.4. The selection of these parameters are made with optimization and this process is described in section 3.2.

### 3.1.1 MCA Blade Generation Procedure

The mathematical procedure of generating an MCA blade is described in detail in the following sections. The steps of the procedure is based on the work done by [2].

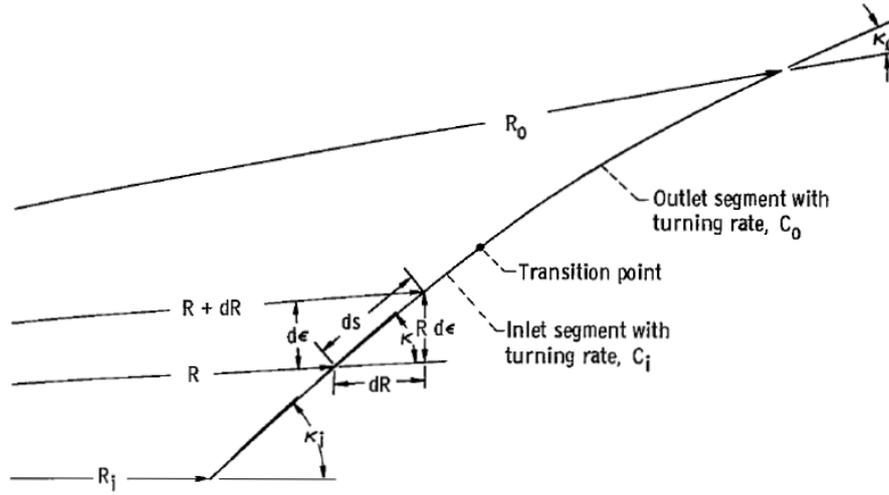


Figure 3.3: Blade element nomenclature [2]

### 3.1.1.1 Mathematical description of constant turning rate segment

In this section  $R$  and  $\epsilon$  are defined as functions of the local blade angle,  $\kappa$ , for a segment with constant turning rate,  $c$ .

For a constant blade turning rate the local blade angle can be described as

$$\frac{d\kappa}{ds} = -c \quad (3.1)$$

or

$$ds = -\frac{d\kappa}{c} \quad (3.2)$$

From Fig 3.3 the differentials of  $R$  and  $\epsilon$  could be written as a function of the infinitesimal element of the arc length,  $ds$

$$dR = \cos \kappa ds \quad (3.3)$$

$$Rd\epsilon = \sin \kappa ds \quad (3.4)$$

Substituting  $ds$  in eq 3.3 and 3.4 with equation 3.2 gives the differentials as functions of the blade angle  $\kappa$ .

$$dR = -\frac{\cos \kappa}{c} d\kappa \quad (3.5)$$

$$d\epsilon = -\frac{\sin \kappa}{Rc} d\kappa \quad (3.6)$$

Integrating equation 3.5 yields

$$R - R_1 = \frac{1}{c} (\sin \kappa_1 - \sin \kappa) \quad (3.7)$$

The turning constant  $c$  in eq 3.7 can after some manipulation be written as

$$c = \frac{\sin \kappa_1 - \sin \kappa}{R - R_1} \quad (3.8)$$



- If  $\kappa \neq \kappa_1$  and  $\xi^2 < 1$

$$\epsilon = \kappa - \kappa_1 + \frac{\xi}{\sqrt{1 - \xi^2}} \left[ \ln \left| \frac{1 - \xi \tan\left(\frac{\kappa}{2}\right) - \sqrt{1 - \xi^2}}{1 - \xi \tan\left(\frac{\kappa}{2}\right) + \sqrt{1 - \xi^2}} \right| - \ln \left| \frac{1 - \xi \tan\left(\frac{\kappa_1}{2}\right) - \sqrt{1 - \xi^2}}{1 - \xi \tan\left(\frac{\kappa_1}{2}\right) + \sqrt{1 - \xi^2}} \right| \right] \quad (3.15)$$

- If  $\kappa \neq \kappa_1$  and  $\xi = \pm 1$

$$\epsilon = \kappa - \kappa_1 \pm \left[ \tan\left(\frac{\pi}{2} \pm \frac{\kappa_1}{2}\right) - \tan\left(\frac{\pi}{4} \pm \frac{\kappa}{2}\right) \right] \quad (3.16)$$

### 3.1.1.2 Equations for thickness

The thickness path is described by a constant angle  $\kappa_n$  which is normal to to the centerline

$$\kappa_n = \kappa_c \pm \frac{\pi}{2} \quad (3.17)$$

Where  $\pm$  denotes path direction to suction- and pressure surface respectively. For a curved thickness path, following equations can be defined

$$dR = \cos \kappa_n dt \rightarrow dt = \frac{dR}{\cos \kappa_n} \quad (3.18)$$

$$d\epsilon = \frac{\sin \kappa_n dt}{R} \quad (3.19)$$

Eq 3.18 in 3.19 and integrate yields

$$R - R_c = t \cos \kappa_n \quad (3.20)$$

$$\epsilon = \epsilon_c + \tan \kappa_n \ln\left(\frac{R}{R_c}\right) \quad (3.21)$$

where t is the path length along the blade centerline. From eq 3.18 and 3.19, the thickness is a function of four variables:  $t$ ,  $R_c$ ,  $\kappa_n$  and  $\epsilon_c$ . There are two solution for  $\kappa_n$ :

- If  $\kappa_n = -\frac{\pi}{2}$

$$\epsilon = \epsilon_c - \frac{t}{R_c} \quad (3.22)$$

- If  $\kappa_n = \frac{\pi}{2}$

$$\epsilon = \epsilon_c + \frac{t}{R_c} \quad (3.23)$$

If none of the above mentioned statements are satisfied, the expression for angular coordinate  $\epsilon$  is given by eq 3.21. The procedure above returns the radius R and angular coordinate  $\epsilon$ . The maximum thickness point can be located on three segments, inlet or outlet, or at the transition point. On the segment of maximum thickness, eq 3.9, 3.12 and 3.8 gives three equations with three unknowns,  $\kappa$ ,  $c$  and  $\xi$ . Due to the complexity of solving these equations explicitly, iterative methods are needed. The first iterative process consist of estimating  $\kappa$  and checking the resulting

$\epsilon$  with the known  $\epsilon$ - coordinate. Second step is to calculate the transition point of the pressure- and suction surface. This is done by finding the intersection of the surface curves with the thickness path of the transition point. Eq 3.14, 3.21 and 3.20 gives three equations for  $\kappa$ ,  $R$  and  $\epsilon$ . The complexity of eq 3.14 makes it difficult to solve explicitly, another iterative process is needed to solve for the unknowns. This iteration process consist of estimating  $R$  which is compared with a known  $R_{tc}$  and calculated  $R_{tc}$  given by 3.24

$$R_{tc} = \frac{R}{\exp [\tan \kappa_{tc} (\epsilon_{tc} - \epsilon)]} \quad (3.24)$$

Where tc represent the transition point at the blade centerline. The last step is to obtain the unknown values of  $\xi, c$  and  $\kappa$  for the surface of the inlet segment. The transition point and trailing- or leading edge point and the angle at the transition point on the pressure and suction surface of the last segment are now known. The first iteration process is used in this step to find the final unknowns.

### 3.1.1.3 Stacking procedure

The stacking is constructed in such a way that the center of area for all blade elements lie on the same stacking line. The first step in the stacking procedure consist of finding the initial positioning of the blade element along the stacking line. An initial approximation is to align the center of area of the blade element along the stacking line. The center of area is calculated by evaluating following integrals

$$R_{sp} = \frac{\int R dA}{\int dA} \quad (3.25)$$

$$\epsilon_{sp} = \frac{\int \epsilon dA}{\int dA} \quad (3.26)$$

$R_{sp}$  and  $\epsilon_{sp}$  is the stacking point for the radius and angular coordinate respectively. The numerator from eq 3.25 and 3.26 can be written as

$$\int R dA = \int_{R_{ic}}^{R_{oc}} R^2 [\epsilon_s (R) - \epsilon_p (R)] dR \quad (3.27)$$

$$\int \epsilon dA = \frac{1}{2} \int_{R_{ic}}^{R_{oc}} R [\epsilon_s^2 (R) - \epsilon_p^2 (R)] dR \quad (3.28)$$

$$\int dA = \int_{R_{ic}}^{R_{oc}} R [\epsilon_s (R) - \epsilon_p (R)] dR \quad (3.29)$$

In order to evaluate the integrals, the angular coordinates,  $\epsilon_s$  and  $\epsilon_p$  needs to be calculated at the transition point of the suction- and pressure side. From eq 3.12,  $\epsilon_{ts}$  and  $\epsilon_{tp}$  can be expressed as

$$\epsilon_p = \epsilon_{tp} + f(\kappa_p, \kappa_{tp}, \xi_{op}, R, R_{tp}) \quad (3.30)$$

$$\epsilon_p = \epsilon_{tp} + f(\kappa_p, \kappa_{tp}, \xi_{ip}, R, R_{tp}) \quad (3.31)$$

$$\epsilon_s = \epsilon_{ts} + f(\kappa_s, \kappa_{ts}, \xi_{os}, R, R_{ts}) \quad (3.32)$$

$$\epsilon_s = \epsilon_{ts} + f(\kappa_s, \kappa_{ts}, \xi_{is}, R, R_{ts}) \quad (3.33)$$

$\kappa_p, \kappa_s, \xi_{ic}, \xi_{oc}$  and radius  $R$  needs to be calculated at the transition point for the inlet and outlet segments of pressure and suction side respectively

$$\xi_{is} = Rc_{is} + \sin \kappa_{is} \quad (3.34)$$

$$\kappa_s = \arcsin(\xi_{is} - Rc_{is}) \quad (3.35)$$

$$\xi_{os} = Rc_{os} + \sin \kappa_s \quad (3.36)$$

$$\kappa_s = \arcsin(\xi_{os} - Rc_{os}) \quad (3.37)$$

The equations above apply for outlet and inlet segment of the centerline at the suction surface. The same equations holds for the pressure side with the difference that at the inlet,  $R_c \leq R_{tc}$  and at the outlet  $R_c > R_{ts}$ . The integrals given by 3.27, 3.28 and 3.29 are very difficult to solve analytically, numerical integration are therefore needed. The numerical procedure of evaluating  $\epsilon_s(R)$  and  $\epsilon_p(R)$  is described below

### Numerical procedure

Eq 3.27, 3.28 and 3.29 needs to be integrated numerically. Define a function with input parameters

$$f_{stack} = f(R_{oc}, R_{ic}, \sigma, R_{ts}, R_{tp}, \xi_{os}, c_{os}, \xi_{op}, c_{op}, \xi_{is}, c_{is}, \xi_{ip}, c_{ip}, \epsilon_{ts}, \kappa_{ts}, \epsilon_{tp}, \kappa_{tp}) \quad (3.38)$$

$\sigma$  is the number of integral points needed for integration. Eq 3.28, 3.29 and 3.30 can be written as a sum

$$\int dA = \sum_{i=1}^{\sigma} f_1 \Delta R \quad (3.39)$$

$$\int RdA = \sum_{i=1}^{\sigma} f_2 \Delta R \quad (3.40)$$

$$\int \epsilon dA = \sum_{i=1}^{\sigma} f_3 \Delta R \quad (3.41)$$

Where  $f_1, f_2$  and  $f_3$  is the integrands of eq 3.28, 3.29 and 3.30.  $\Delta R$  can be written as

$$\Delta R = \frac{R_{oc} - R_{ic}}{\sigma - 1} \quad (3.42)$$

$$R = R_{ic} \quad (3.43)$$

The procedure of obtaining  $\kappa$  and  $\epsilon$  for suction and pressure side is described below

- If  $R \geq R_{ts}$

$$\kappa_s = \arcsin(\xi_{os} - Rc_{os}) \quad (3.44)$$

$$\epsilon_s = \epsilon_{ts} + f_{\epsilon}(\kappa_s, \kappa_{ts}, \xi_{os}, R, R_{ts}) \quad (3.45)$$

Else

$$\kappa_s = \arcsin(\xi_{is} - Rc_{is}) \quad (3.46)$$

$$\epsilon_s = \epsilon_{ts} + f_{\epsilon}(\kappa_s, \kappa_{ts}, \xi_{is}, R, R_{ts}) \quad (3.47)$$

- If  $R \geq R_{tp}$

$$\kappa_p = \arcsin(\xi_{op} - Rc_{op}) \quad (3.48)$$

$$\epsilon_p = \epsilon_{tp} + f(\kappa_p, \kappa_{tp}, \xi_{op}, R, R_{tp}) \quad (3.49)$$

Else

$$\kappa_p = \arcsin(\xi_{ip} - Rc_{ip}) \quad (3.50)$$

$$\epsilon_p = \epsilon_{tp} + f(\kappa_p, \kappa_{tp}, \xi_{ip}, R, R_{tp}) \quad (3.51)$$

The integral values can now be calculated by using a suitable numerical integration method. The stacking points,  $\epsilon_{sp}$  and  $R_{sp}$  can now be obtained.

#### Calculating variables needed for each blade element

Cone angle,  $\alpha$  can be defined as

$$\alpha = \left( \frac{r_{oc} - r_{ic}}{z_{oc} - z_{ic}} \right) \quad (3.52)$$

Where  $z_{oc} - z_{ic}$  is the distance from leading- to trailing edge of the blade centerline in the  $z$ -direction.  $r_{oc} - r_{ic}$  is the distance from leading- to trailing edge of the blade centerline in radial coordinates. The  $R$  coordinate of the leading edge center can be expressed as

$$R_{ic} = \frac{r_{ic}}{\sin \alpha} \quad (3.53)$$

From eq 3.53 it can be seen that eq 3.53 is not defined for  $\alpha = 0$ , a small cone angle is employed for calculating  $R$ -coordinates for leading, trailing and transition points on the blade centerline. The  $R$ -coordinates for trailing, leading and transition points are given by

$$R_{tc} = R_{ic} + \frac{z - z_{tc}}{\cos \alpha} \quad (3.54)$$

$$R_{mc} = R_{ic} + \frac{z - z_{mc}}{\cos \alpha} \quad (3.55)$$

$$R_{oc} = R_{ic} + \frac{z - z_{oc}}{\cos \alpha} \quad (3.56)$$

There are three possibilities for maximum thickness point,  $z - z_{mc}$ :

- If  $z - z_{mc} < z - z_{tc}$ : Maximum thickness point,  $z_{mt}$  belong to inlet segment
- If  $z - z_{mc} > z - z_{tc}$ : Maximum thickness point,  $z_{mt}$  belong to outlet segment
- If  $z - z_{mc} = z - z_{tc}$ : Maximum thickness point coincide with the transition point.

Now, the turning-rate constant,  $c$  and  $\xi$  can be obtained from eq 3.8 and 3.9 for leading- and trailing edge on the blade centerline

$$c_{ic} = \frac{\sin \kappa_{ic} - \sin \kappa_{tc}}{R_{tc} - R_{ic}} \quad (3.57)$$

$$c_{oc} = \frac{\sin \kappa_{tc} - \sin \kappa_{oc}}{R_{oc} - R_{tc}} \quad (3.58)$$

$$\xi_{ic} = R_{tc}c_{ic} + \sin \kappa_{tc} \quad (3.59)$$

$$\xi_{oc} = R_{tc}c_{oc} + \sin \kappa_{tc} \quad (3.60)$$

In order to make the calculation of angular coordinates,  $\epsilon_{tc}$  and  $\epsilon_{oc}$  easier, the angular coordinate for the transition point could be set to zero ( $\epsilon_{ic} = 0$ ). This is due to that the blade element are referenced from the leading edge. Angular coordinates for trailing edge and transition point can now be calculated for leading and trailing edge respectively

$$\epsilon_{tc} = \epsilon_{ic} + f_{\epsilon}(\kappa_{tc}, \kappa_{ic}, \xi_{ic}, R_{tc}, R_{ic}) \quad (3.61)$$

$$\epsilon_{oc} = \epsilon_{tc} + f_{\epsilon}(\kappa_{oc}, \kappa_{tc}, \xi_{oc}, R_{oc}, R_{tc}) \quad (3.62)$$

R and angular coordinates for pressure and suction side at the inlet and outlet can now be calculated

$$R_{is}, \epsilon_{is} = f_t\left(\kappa_{ic} + \frac{\pi}{2}, R_{ic}, \frac{t_i}{2}, \epsilon_{ic}\right) \quad (3.63)$$

$$R_{ip}, \epsilon_{ip} = f_t\left(\kappa_{ic} - \frac{\pi}{2}, R_{ic}, \frac{t_i}{2}, \epsilon_{ic}\right) \quad (3.64)$$

$$R_{os}, \epsilon_{os} = f_t\left(\kappa_{oc} + \frac{\pi}{2}, R_{oc}, \frac{t_o}{2}, \epsilon_{oc}\right) \quad (3.65)$$

$$R_{op}, \epsilon_{op} = f_t\left(\kappa_{oc} - \frac{\pi}{2}, R_{oc}, \frac{t_o}{2}, \epsilon_{oc}\right) \quad (3.66)$$

$f_t$  is a function of points of known thickness. Blade angle  $\kappa$  at the point of maximum thickness on either pressure or suction side is equal to the angle at maximum thickness point on the centerline,  $\kappa_{mc} = \kappa_{ms} = \kappa_{mp} = \kappa_m$ . Equations for maximum thickness point, R and angular coordinates at the maximum thickness point can now be established

- If maximum thickness point belong to transition point

$$\kappa_{mc} = \kappa_{tc} \quad (3.67)$$

$$\epsilon_{mc} = \epsilon_{tc} \quad (3.68)$$

- If maximum thickness point belong to outlet segment

$$\kappa_{mc} = \arcsin(\xi_{os} - R_{mc}c_{oc}) \quad (3.69)$$

$$\epsilon_{mc} = \epsilon_{oc} + f_{\epsilon}(\kappa_{mc}, \kappa_{oc}, \xi_{oc}, R_{mc}, R_{oc}) \quad (3.70)$$

- If maximum thickness point belong to inlet segment

$$\kappa_{mc} = \arcsin(\xi_{ic} - R_{mc}c_{ic}) \quad (3.71)$$

$$\epsilon_{mc} = \epsilon_{ic} + f_{\epsilon}(\kappa_{mc}, \kappa_{ic}, \xi_{ic}, R_{mc}, R_{ic}) \quad (3.72)$$

The surface curves for segments containing the maximum thickness point can now be established for inlet, outlet and transition points. In order to find the curves for the different segments, the correct  $\kappa$  must be iterated using eq 3.8, 3.9 and 3.12. Functions for  $\kappa$  with input variables for the inlet segment at pressure and suction

surface respectively

$$f_{\kappa s} = f(\kappa_{ic}, \epsilon_{is}, R_{is}, \kappa_m, \epsilon_{ms}, R_{ms}) \quad (3.73)$$

$$f_{\kappa p} = f(\kappa_{ic}, \epsilon_{ip}, R_{ip}, \kappa_m, \epsilon_{mp}, R_{mp}) \quad (3.74)$$

$\kappa$ ,  $c$  and  $\epsilon$  for suction and pressure surface can now be obtained for the inlet segment

$$\kappa_{is}, c_{is}, \epsilon_{is} = f_{\kappa s} \quad (3.75)$$

$$\kappa_{ip}, c_{ip}, \epsilon_{ip} = f_{\kappa p} \quad (3.76)$$

To find the transition point coordinates at the inlet segment, eq 3.10, 3.12 and 3.21 are used to iterate a correct  $R$  and  $\epsilon$  for pressure and suction side respectively

$$f_{Rs} = f(R_{tc}, \xi_{is}, c_{is}, \kappa_m, R_{ms}, \kappa_{tc}, \epsilon_{tc}, R_{tc}, \epsilon_{ms}) \quad (3.77)$$

$$f_{Rp} = f(R_{tc}, \xi_{ip}, c_{ip}, \kappa_m, R_{mp}, \kappa_{tc}, \epsilon_{tc}, R_{tc}, \epsilon_{mp}) \quad (3.78)$$

$R$ ,  $\epsilon$  and  $\kappa$  can now be obtained for pressure and suction surface at the inlet segment

$$R_{ts}, \epsilon_{ts}, \kappa_{ts} = f_{Rs} \quad (3.79)$$

$$R_{tp}, \epsilon_{tp}, \kappa_{tp} = f_{Rp} \quad (3.80)$$

Coordinates for the outlet segment is done the same way as for the inlet. Iteration using eq 3.8, 3.9 and 3.12 is used to find the correct  $\kappa$  at pressure and suction side

$$f_{\kappa s} = f(\kappa_{oc}, \epsilon_{os}, R_{os}, \kappa_{ts}, \epsilon_{ts}, R_{ts}) \quad (3.81)$$

$$f_{\kappa p} = f(\kappa_{oc}, \epsilon_{op}, R_{op}, \kappa_{tp}, \epsilon_{tp}, R_{tp}) \quad (3.82)$$

$\kappa$ ,  $c$  and  $\xi$  can now be obtained for pressure and suction surface at the outlet segment

$$\kappa_{os}, c_{os}, \epsilon_{os} = f_{\kappa s} \quad (3.83)$$

$$\kappa_{op}, c_{op}, \epsilon_{op} = f_{\kappa p} \quad (3.84)$$

If the maximum thickness point coordinates is the same as the transition point coordinates, then:

$\kappa_{tp} = \kappa_{tc}$ ,  $\kappa_{ts} = \kappa_{tc}$ ,  $R_{tc} = R_{ms}$ ,  $R_{tp} = R_{mp}$ ,  $\epsilon_{ts} = \epsilon_{ms}$ ,  $\epsilon_{tp} = \epsilon_{mp}$ .  $\kappa$ ,  $c$ ,  $\xi$  for the inlet and outlet segment is given by

$$\kappa_{os}, c_{os}, \epsilon_{os} = f_{\kappa s} \quad (3.85)$$

$$\kappa_{op}, c_{op}, \epsilon_{op} = f_{\kappa p} \quad (3.86)$$

If the outlet segment contain the maximum thickness point,  $\kappa$ ,  $c$  and  $\xi$  for suction and pressure surface is given by eq 3.85 and 3.86. The transition point coordinates for pressure and suction surface is given by eq 3.79 and 3.80.  $\kappa$ ,  $c$  and  $\xi$  for the inlet segment for the pressure and suction surface is given by eq 3.74 and 3.75.

### Second step in the stacking procedure

Second step in the stacking procedure consist of finding the cylindrical coordinates of the blade element stacking points,  $\theta_{sp}, z_{sp}$  relative to a common reference. The stacking point in the axial direction can be defined as

$$z_{sp} = z_{sp,h} + (r_{sp} - r_{sp,h}) \tan \lambda \quad (3.87)$$

Where h denotes hub - blade - element value.  $r_{sp}$  can be defined as

$$r_{sp} = R_{sp} \sin \alpha \quad (3.88)$$

$R_{sp}$  is the radial stacking point given by eq 3.25. The stacking point for the angular coordinate is given by eq 3.26. The stacking point in  $\theta$ - direction is expressed as

$$\theta_{sp} = \theta_{sp,h} + \delta \quad (3.89)$$

$$\Delta\theta_{sp,ic} = \frac{\int \epsilon dA}{\int dA \sin \alpha} \quad (3.90)$$

Where  $\delta$  is defined as

$$\delta = \arcsin \left[ \frac{r_{sp,h}}{r_{sp}} \left( \frac{\tan \eta}{1 + \tan^2 \eta} \right) \left[ \sqrt{\left( \frac{r_{sp}}{r_{sp,h}} \right)^2 (1 + \tan^2 \eta) - \tan^2 \eta} - 1 \right] \right] \quad (3.91)$$

$\lambda$  is the lean angle positive in the z-direction and  $\eta$  is the lean angle positive in the  $\theta$ -direction, illustrated in Fig 3.5

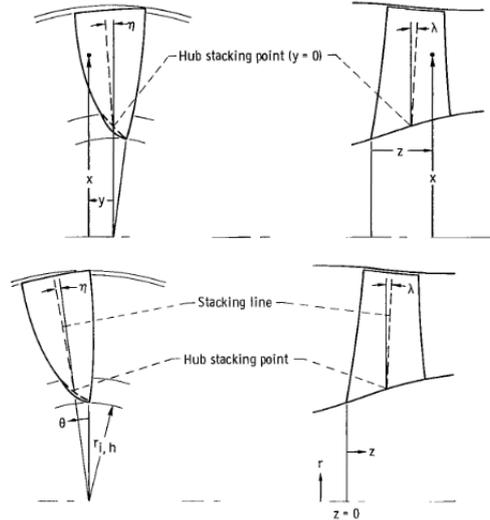


**Figure 3.5:** *Cylindrical and cartesian coordinate system for the blade [2]*

Now, following coordinates can be calculated

$$(R_{oc}, R_{ic}, R_{tc}, R_{mc}, R_{ts}, R_{tp}, \xi_{os}, c_{os}, \xi_{op}, c_{op}, \epsilon_{ts}, \kappa_{ts}, \epsilon_{tp}, \kappa_{tp}, R_{sp}, \epsilon_{mc}, \Delta\theta_{sp,ic}, \int \epsilon dA, \int r dA, \int dA, \alpha, r_{sp}, R_{is}, R_{ip}, R_{os}, R_{op}, \epsilon_{is}, \epsilon_{ip}, \epsilon_{os}, \epsilon_{op}, \epsilon_{tc}, R_{mp}, \epsilon_{mp}, R_{ms}, \epsilon_{ms}, \epsilon_{oc}, \xi_{is}, \xi_{ip}, c_{ic}, c_{oc}, c_{is}, c_{ip}, \kappa_{is}, \kappa_{ip})$$

### Third step in the stacking procedure

Third step in the stacking procedure consist of calculating the  $x$ ,  $y$  and  $z$  coordinates of the blade elements. This is done by converting the obtained  $R$  and  $\epsilon$  values using the following conversion equations

$$x = R \sin \alpha \cos \left( \frac{\epsilon}{\sin \alpha} + \theta_{ic} - \theta_{sp,h} \right) \quad (3.92)$$

$$y = R \sin \alpha \sin \left( \frac{\epsilon}{\sin \alpha} + \theta_{ic} - \theta_{sp,h} \right) \quad (3.93)$$

$$z = z_{sp} - (R_{sp} - R) \cos \alpha \quad (3.94)$$

where the  $z$  value for the stacking point is  $z_{sp}$  and the cylindrical coordinate of the center at the leading edge radius is

$$\theta_{ic} = \theta_{sp} - (\theta_{sp} - \theta_{ic}) = \theta_{sp,h} + \delta - \frac{\epsilon_{sp}}{\sin \alpha} \quad (3.95)$$

Since  $R$  and  $\epsilon$  have already been calculated for the leading edge, transition, maximum thickness and trailing edge points. The conversion to  $x$ ,  $y$  and  $z$  for these points can now be carried out. The most convenient approach is to calculate the blade surface curves at constant  $z$  values. Therefore, the remaining points on the blade surfaces are calculated by dividing the  $z$  interval of the complete blade into constant segments. The upper and lower bounds of the  $z$  interval for the complete blade are found by searching the leading and trailing edge coordinates for both surfaces of all blade elements. Before the cartesian coordinates of the blade surfaces can be calculated it is first necessary to calculate  $R$  and  $\epsilon$  coordinates at the established  $z$  segments. To calculate  $\epsilon$  the local blade angle,  $\kappa$  is needed. Where  $\epsilon$  is calculated with equation 3.12 and using the known values at the transition point as reference. The equations for  $R$ ,  $\epsilon$  and  $\kappa$  at the surfaces are then given by eq 3.56, 3.12 and 3.10

- For the centerline

$$R_c = R_{ic} + \frac{z - z_{ic}}{\cos \alpha} \quad (3.96)$$

- $z$  values belonging to the inlet segment

$$\kappa_c = \arcsin (\xi_{ic} - R_c C_{ic}) \quad (3.97)$$

$$R_p, \epsilon_p = f (R_c, C_{ip}, \xi_{ip}, \kappa_{tp}, R_{tp}, \epsilon_{tp}) \quad (3.98)$$

$$R_s, \epsilon_s = f (R_c, C_{is}, \xi_{is}, \kappa_{ts}, R_{ts}, \epsilon_{ts}) \quad (3.99)$$

- $z$  values belonging to the outlet segment

$$\kappa_c = \arcsin (\xi_{oc} - R_c C_{oc}) \quad (3.100)$$

$$R_p, \epsilon_p = f (R_c, C_{op}, \xi_{op}, \kappa_{tp}, R_{tp}, \epsilon_{tp}) \quad (3.101)$$

$$R_s, \epsilon_s = f (R_c, C_{os}, \xi_{os}, \kappa_{ts}, R_{ts}, \epsilon_{ts}) \quad (3.102)$$

Now that  $R$  and  $\epsilon$  values are known at each  $z$  value for every blade element the  $x$  and  $y$  coordinates can be calculated with equations eq 3.92 and 3.93.

#### Fourth step in the stacking procedure

The fourth step in the stacking procedure consists of interpolating the blade element surface coordinates. For each  $x$  value the  $y$  and  $z$  coordinates defines the blade section profile. The  $x$  values used are the previously calculated stacking points. The  $y$  coordinates are interpolated using second order Lagrangian for all  $x$  values and on each surface line with same  $z$  value. The blade element coordinates,  $[x_{1,(p,s)}, y_{1,(p,s)}, z_j]$ ,  $[x_{2,(p,s)}, y_{2,(p,s)}, z_j]$  and  $[x_{3,(p,s)}, y_{3,(p,s)}, z_j]$  are consecutive points along the  $z$ -axis. The eq for  $y_{(p,s)}$  then becomes

$$y_{(p,s)} = y_{1,(p,s)}W_1 + y_{2,(p,s)}W_2 + y_{3,(p,s)}W_3 \quad (3.103)$$

where

$$W_1 = \frac{[x - x_{2,(p,s)}][x - x_{3,(p,s)}]}{[x_{1,(p,s)} - x_{2,(p,s)}][x_{1,(p,s)} - x_{3,(p,s)}]} \quad (3.104)$$

$$W_2 = \frac{[x - x_{1,(p,s)}][x - x_{3,(p,s)}]}{[x_{2,(p,s)} - x_{1,(p,s)}][x_{2,(p,s)} - x_{3,(p,s)}]} \quad (3.105)$$

and

$$W_3 = \frac{[x - x_{1,(p,s)}][x - x_{2,(p,s)}]}{[x_{3,(p,s)} - x_{1,(p,s)}][x_{3,(p,s)} - x_{2,(p,s)}]} \quad (3.106)$$

Using this,  $y_p$  and  $y_s$  are calculated for each  $z$ .

#### Fifth step in the stacking procedure

This step consists of calculating the centers of area for blade sections. The center of area coordinates are calculated by dividing the area moments by the area of the blade section. Both area and area moments are calculated by numerical integration. The equations for area and area moments are as follows

$$A = \int_{z_{min}}^{z_{max}} \int_{y_p}^{y_s} dy dz = \int_{z_{min}}^{z_{max}} [y_s(z) - y_p(z)] dz \quad (3.107)$$

$$y_{ca}A = \int_{z_{min}}^{z_{max}} \int_{y_p}^{y_s} y dy dz = \int_{z_{min}}^{z_{max}} \frac{1}{2} [y_s^2(z) - y_p^2(z)] dz \quad (3.108)$$

$$z_{ca}A = \int_{z_{min}}^{z_{max}} \int_{y_p}^{y_s} z dy dz = \int_{z_{min}}^{z_{max}} z [y_s(z) - y_p(z)] dz \quad (3.109)$$

#### Sixth step in the stacking procedure

This last step in the stacking differ from the procedure followed in [2]. Instead of using interpolating and tedious iterations, the blade elements are stacked by calculation.

Now that all the blade elements have been calculated and positioned on their conical surface they are moved so that their center of area coincides with the stacking line. Each blade element have two possible motions on the cone surface, these are

calculated to correctly place the blade elements. Firstly, the blade elements can be displaced along the  $z$  axis, meaning the whole cone moves along  $z$ . Secondly, the blade elements can be rotated  $\theta$ , meaning that the cone is rotated around its own axis. The translation and rotation directions are visualized in Fig 3.5. The stacking point for each blade element is calculated by the intersection between a cylinder with radius  $r_{ca}$ , illustrated in Fig 3.6, and the stacking line.

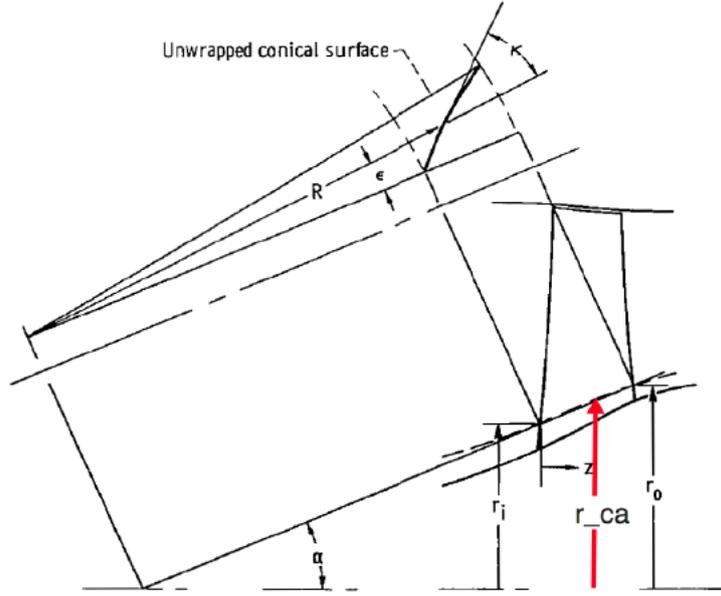


**Figure 3.6:** *Conical coordinate system with blade element center of area radius illustrated*

Since the radius of the stacking point,  $r_{ca}$ , is independent of the offsets  $z$  and  $\theta$  the equation of a cylinder with radius  $r_{ca}$  can be written in the cartesian coordinate system as

$$x = r_{ca} \cos(\theta) \quad (3.110)$$

$$y = r_{ca} \sin(\theta) \quad (3.111)$$

$$z = z \quad (3.112)$$

Using the notation  $x_{ca,h}$  and  $y_{ca,h}$  for the stacking point coordinates of the hub blade element, the stacking line in cartesian coordinate system shown in Fig 3.5 can be written as

$$x = x_{ca,h} + \frac{z - z_{ca,h}}{\tan(\lambda)} \quad (3.113)$$

$$y = y_{ca,h} + (x - x_{ca,h}) \tan(\eta) = y_{ca,h} + \frac{z - z_{ca,h}}{\tan(\lambda)} \tan(\eta) \quad (3.114)$$

$$z = z \quad (3.115)$$

Imposing the condition that  $x^2 + y^2 = r_{ca}^2$  in eq 3.113 and 3.114, the  $z$  coordinate for the stacking point can be calculated for each blade element as

$$A_0 = x_{ca,h}^2 + y_{ca,h}^2 \quad (3.116)$$

$$A_1 = \frac{2(x_{ca,h} + y_{ca,h} \tan(\eta))}{\tan(\lambda)} \quad (3.117)$$

$$A_2 = \frac{1 + \tan^2(\eta)}{\tan^2(\lambda)} \quad (3.118)$$

$$C_1 = A_0 - A_1 z_{ca,h} + A_2 z_{ca,h}^2 - r_{ca}^2 \quad (3.119)$$

$$C_2 = A_1 - 2A_2 z_{ca,h} \quad (3.120)$$

$$C_3 = A_2 \quad (3.121)$$

$$C_3 z^2 + C_2 z + C_1 = 0 \quad (3.122)$$

With the obtained  $z$  values from equations 3.116 to 3.122, the corresponding  $x$  and  $y$  coordinates of the intersection between the stacking line and the cylinder can be obtained from eq 3.113 to 3.115. Out of the two  $z$  solutions obtained from eq 3.122 the interesting one is the one which has a corresponding  $x$  coordinate greater than  $x_{ca,h}$ . The  $\theta$  coordinate is then obtained from eq 3.110 to 3.111. Now that the correct  $\theta$  and  $z$  are known, comparing them with the original values obtained from the first iteration of the original procedure, the offsets in  $z$  and  $\theta$  can be calculated. Applying the offsets for all blade element points the correct positioning for each blade element is found.

### Connecting pressure and suction surfaces

The final step is to connect the blade surfaces with a circular arc. A circle is fitted at the leading edge so that it is tangent to the lines from the pressure and suction side. The same procedure is made for the trailing edge.

## 3.2 Optimization

In this chapter the search for optimal blade properties, ones defined in section 3.1, is described.

### 3.2.1 Blade Representation

Before the optimization is initialized, it must be certain that the objects can be matched. To be able to make the comparison of the MCA blade represented on conical surfaces with another blade, not necessarily represented by cones, it is required to represent the reference blade by airfoils described by the same conical surface representation. In other words, to ensure the cones used in the MCA blade and the blade used for comparison have the same cone half-angle and are equally positioned. This is achieved by having the leading- and trailing-edge radius  $r_{ic}$  and  $r_{oc}$ , together

with the axial length,  $z_{oc}$ , fixed. This means that from the 11 blade properties, described in section 3.1, three will remain constant reducing the number of parameters required to be optimized to eight per spanwise blade element or 120 in total. The reference blade can now be intersected with the cones for each span yielding a set of airfoils that represents the blade on a conical surface. The intersects are made at 15 spans to mimic the construction of the reference blade. The intersection is illustrated in Fig 3.7.

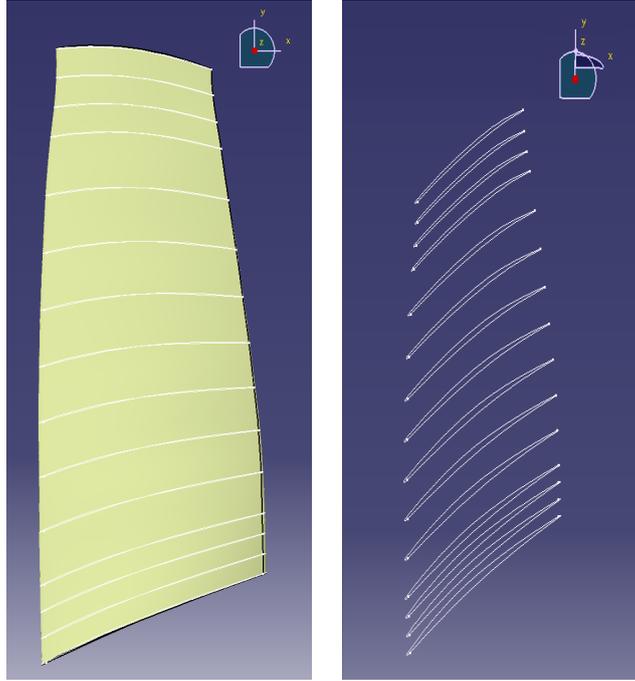


**Figure 3.7:** *Reference blade represented by airfoils on conical surfaces*

#### 3.2.2 Objective Functions

For the optimizer to evaluate solutions, objective functions are required. Since the objective of the optimization is to recreate the reference blade with an MCA blade using a geometrical approach, the objective functions are formulated with the aim of evaluating the geometrical deviation.

Due to the MCA generation requiring the selection of the 5 blade properties for each of the 15 spans, the optimization becomes multi-variable with 75 variables. Where a set of 75 variables forms 15 individual blade elements stacked at a common stacking line, which are then compared to the 15 intersects made of the reference blade. The problem is inherently single objective since it can be reduced to distance between points in two point clouds. However, instead of trying to tie the exact position on each MCA blade element which matches the position on the reference blade elements. The problem is simplified by comparing each blade element before they are stacked. The individual blade elements are best compared in the  $r\theta - x$  plane, illustrated in 2.3, where they are translated to the same position in axial direction

making the comparison at each  $x$  position entirely in  $r\theta$ . The comparison between blades are done with pressure and suction side independently. By comparing the blade elements before the stacking simplifies the comparison but unfortunately adds another objective function, deviation in stacking, making it multi-objective as well. The two objectives can be formulated as:

$$\text{Minimize: } f_1(\mathbf{x}) = \bar{d}$$

$$\text{Minimize: } f_2(\mathbf{x}) = d_{cones}$$

Where  $d_{cones}$  denotes the largest cone deviation, of all blade elements, in axial direction and  $\bar{d}$  denotes the average distance between the blade profiles, first averaged for distance between all points on two blade elements then averaged for each span. The objectives can be mathematical described as

$$\bar{d} = \frac{\sum_1^m \frac{\sum_i^n (r_i\theta_i - r_j\theta_j)}{n}}{m} \quad (3.123)$$

$$d_{cones} = \max(|x_i - x_j|) \quad (3.124)$$

where index  $i$  denotes points on the reference blade and  $j$  the corresponding point on the MCA blade in the same  $x$  position. The points on the MCA blade have been interpolated to match the  $x$  position of the reference blade.  $n$  represent the number of points on each blade element and  $m$  represent the number of spans. The difference between  $r_i\theta_i$  and  $r_j\theta_j$  corresponds to the circumferential distance between the two blade profiles. For the second objective function,  $x_i$  and  $x_j$  are the same point on the MCA and reference blade, i.e trailing or leading edge, for each span.

### 3.2.3 Multi-objective optimization

Optimization of more than one objective function is known as multi-objective optimization. In this type of optimization a trade-off between the conflicting objective functions needs to be made. The optimizer cannot find a single solution that optimizes all the objective functions. Instead several solutions are found which trades one objective for another. When none of the objective functions can be improved without sacrificing another, the solutions are said to be pareto-optimal.

### 3.2.4 Optimizer

The algorithm used for the optimization is a Non-dominated Sorting Genetic Algorithm (NSGA-II). It is based on evolutionary processes where it tries to mimic the process of natural evolution. Each variable to optimize are binary encoded in an array called chromosomes. Each element in the chromosomes is called a gene. The algorithm will deal with generations where a generation consists of populations where each population consists of individuals which in turn consists of all the variables to optimize which are defined by the chromosomes. One individual will then be one design to consider. The chromosomes are decoded to assign a value to the variable. The genes are randomized and from there, the population is initialized

from a predefined population size. From the population a tournament selection is made between two randomly selected individuals to determine which shall form the next generation. Crossover, which generates new individuals to the next generation from the selected individuals of the tournament. Mutation is also included where a single gene in an individual is changed. Elitism is also used to preserve the best individuals of each generation. In the last step, the parent and offspring population are combined where a fast non-dominated sorting and a crowding distance procedure is implemented to rank the combined population with the best  $N$  individuals, which are selected as new parent population [10].

### 3.2.5 Variable Range

The variables to optimize are blade properties that define the MCA blade. These variables include local blade angle,  $\kappa$ , local thickness,  $t$ , and two axial distances from the hub blade element leading edge to the maximum thickness and transition point on the centerline. The blade angles and thicknesses are for three critical points on the centerline, inlet, outlet and maximum thickness. In the optimization a range is defined for each variable which will determine the time it takes to find an optimal design. Therefore, finding a good range for the optimization variables is vital. The chosen ranges are found by iteration where the values for thicknesses are calculated from a preliminary camber line. The preliminary camberline is defined by half the distance between pressure and suction side. The preliminary camberline is illustrated in Fig 3.8. The range for local blade angles  $\kappa$  at the three points are initialized by intuition. After the initial ranges are defined they are optimized in the NSGA-II where each blade element is run individually. From the pareto front, new ranges are found and this process is iterated until a satisfactory narrow range is achieved. When the final variable ranges are found the complete blade is optimized in the NSGA-II.

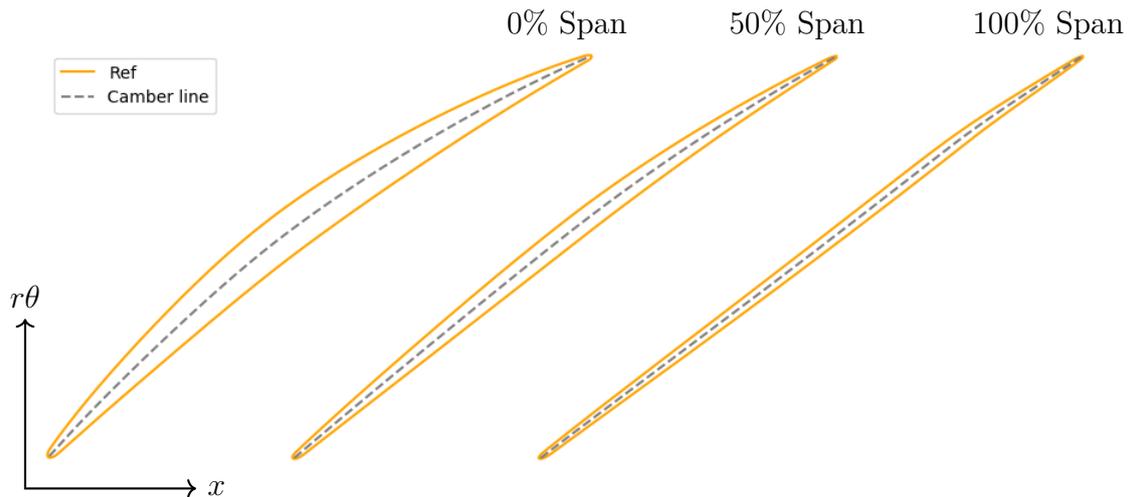


**Figure 3.8:** Preliminary camberline used to determine initial range of thickness and axial distance of transition/maximum thickness point

### 3.2.6 Optimization Framework

The framework developed for this optimization is illustrated in 3.9. The variables are initialized inside the virtual loop with a randomized population which with the help of the NSGA-II finds the pareto-optimal designs. The found designs are added to the variable database. From the variable database, MCA blades are generated. The blades are then evaluated by the objective functions which enables the pareto front to be extracted. If the designs are not converged the designs are run through the virtual loop again to push down the pareto front.

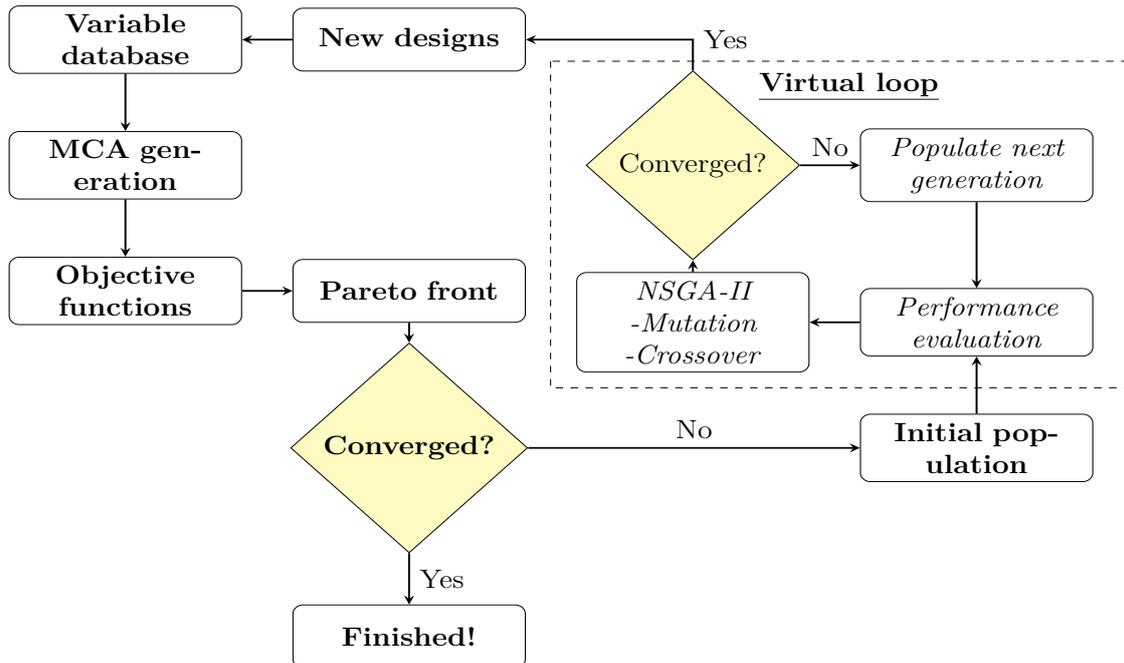


Figure 3.9: Flowchart of optimization procedure

### 3.3 CFD

#### 3.3.1 Numerical Method

The solver used to solve the Favre-filtered, Reynolds-averaged unsteady Navier - Stokes equations is called G3D::Flow, the code is an in-house code developed at Chalmers University of Technology. G3D::Flow is a compressible solver used in a wide range of turbomachinery applications. It is a finite-volume, density-based solver using a three-stage Runge-Kutta time marching method. Diffusive fluxes are computed using second order central differencing scheme in space and the convective fluxes are computed using third order upwind scheme, taking the propagating direction of the flow into consideration. In order to capture the effects of shocks, extra artificial numerical dissipation is added. Discretization of eq 2.50 is based on the finite-volume method. Integrating over an arbitrary control volume ,  $\Gamma$ , yields

$$\int_{\Gamma} \frac{\partial \mathcal{Q}}{\partial t} dV + \int_{\Gamma} \frac{\partial \mathcal{F}_j}{\partial x_j} dV = \int_{\Gamma} \mathcal{H} dV \quad (3.125)$$

Applying the divergence theorem on the flux vector,  $\mathcal{F}_j$  in eq 3.125, and taking the average of the state vector,  $\mathcal{Q}$  and  $\mathcal{H}$  respectively yields

$$\frac{\partial \bar{\mathcal{Q}}}{\partial t} \Delta V + \int_{\partial \Gamma} \mathcal{F}_j \hat{n} dS_j = \bar{\mathcal{H}} \Delta V \quad (3.126)$$

Where the product  $\hat{n} dS_j$  is the net flux out of the control surface,  $\partial \Gamma$ . The surface integral in eq 3.126 can over a control volume cell be approximated as

$$\int_{\partial \Gamma} \mathcal{F}_j \hat{n} dS_j = \sum_{i=1}^n [\mathcal{F}_j S_j]_i \quad (3.127)$$

Where n is all cell faces in the grid. Combining eq 3.126 and 3.127 yields

$$\frac{\partial \bar{\mathcal{Q}}}{\partial t} \Delta V + \sum_{i=1}^n [\mathcal{F}_j S_j]_i = \bar{\mathcal{H}} \Delta V \quad (3.128)$$

The flux term is approximated is by dividing the convective- and diffusive fluxes identified from eq 2.52

$$\mathcal{F}_j = \begin{bmatrix} \bar{\rho} \tilde{u}_i \\ \bar{\rho} \tilde{u}_i \tilde{u}_j + \bar{p} \delta_{ij} \\ \bar{\rho} \tilde{e}_0 \tilde{u}_j + \bar{p} \tilde{u}_j \\ \bar{\rho} \tilde{k} \tilde{u}_j \\ \bar{\rho} \tilde{\varepsilon} \tilde{u}_j \end{bmatrix} + \begin{bmatrix} 0 \\ -\tau_{ij} \\ -c_p \left( \frac{\mu}{Pr} + \frac{\mu_t}{Pr_t} \right) \frac{\partial T}{\partial x_j} - \tilde{u}_i \tau_{ij} \\ - \left( \mu + \frac{\mu_t}{\sigma_k} \right) \frac{\partial k}{\partial x_j} \\ - \left( \mu + \frac{\mu_t}{\sigma_\varepsilon} \right) \frac{\partial \varepsilon}{\partial x_j} \end{bmatrix} \quad (3.129)$$

### 3.3.1.1 Time Stepping

The system of ODE:s from eq 3.129 can in vector form be expressed as

$$\frac{\partial \mathbf{Q}}{\partial t} = \mathbf{F}(\mathbf{Q}) \quad (3.130)$$

Where  $\mathbf{Q}$  contains all DOF in every cell and  $\mathbf{F}(\mathbf{Q})$  is the time derivative of  $\mathbf{Q}$  from the flux term approximations. Eq 3.130 is solved explicitly in time using a three-stage Runge-Kutta time marching method. The time stepping algorithm is outlined below [11]

$$\mathbf{Q}^* = \mathbf{Q}^n + \Delta t \mathbf{F}(\mathbf{Q}^n) \quad (3.131)$$

$$\mathbf{Q}^{**} = \mathbf{Q}^n + \frac{1}{2} \Delta t \mathbf{F}(\mathbf{Q}^n) + \frac{1}{2} \Delta t \mathbf{F}(\mathbf{Q}^*) \quad (3.132)$$

$$\mathbf{Q}^{n+1} = \mathbf{Q}^n + \frac{1}{2} \Delta t \mathbf{F}(\mathbf{Q}^n) + \frac{1}{2} \Delta t \mathbf{F}(\mathbf{Q}^{**}) \quad (3.133)$$

Where  $\mathbf{Q}^n = \mathbf{Q}(t_n)$  and  $\mathbf{Q}^{n+1} = \mathbf{Q}(t_{n+1})$ .  $\Delta t$  is the time step of the solver.  $n$  denotes the previous time step and  $n+1$  denote the next time step. Superscripts  $*$  and  $**$  denote sub-time steps.

### 3.3.1.2 Boundary conditions

Boundary condition is set as subsonic inflow for the inlet, while the outflow boundary conditions are based on the method of characteristic. The outflow variables are expressed in conservative form while the inflow variables are expressed in primitive form.

#### Inlet

- Total temperature,  $T_0$ .
- Total pressure,  $p_0$ .
- Velocity component in the axial, radial and tangential directions,  $\tilde{u}_x, \tilde{u}_\theta, \tilde{u}_r$ .
- Turbulent kinetic energy,  $k$ .
- Turbulent kinetic energy dissipation rate,  $\varepsilon$ .

#### Outlet

- For three - dimensional unsteady turbulent flows, wave reflections in the domain pose problems of numerical instability, and must therefore be carefully monitored. In order to improve numerical stability, a non-reflective boundary condition is applied allowing these acoustic waves to leave the domain. This boundary condition work as a static pressure boundary condition.

#### Blade surface

At the blade surface, following boundary conditions are specified

- Velocity vector,  $\tilde{u}_i$ . The tangential velocity component is placed at the first cell adjacent of the wall using wall functions. The normal velocity component is set to zero.
- The wall is assumed to be adiabatic, i.e zero heat flux at the surface. The normal component of temperature is therefore set to zero.

- Turbulent kinetic energy,  $k$ , and turbulent kinetic energy dissipation rate,  $\varepsilon$  is applied at the first cell adjacent to the blade surface using wall functions.
- Normal component of static pressure is set to zero, ensuring no flow through the wall.

#### **Periodic surface**

For the surfaces, the flow is assumed to be rotational periodic. A periodic rotational boundary condition is therefore applied.

#### **Mixing planes**

The interface between the rotational and stationary domains were treated by implementing mixing planes with non-reflective properties. Applying mixing plane as a boundary condition ensured a steady flow solution through the turbomachine [21]. The basis of mixing plane boundary condition is to first divide the interface into circumferential sections by the grid lines at approximately constant radius. Next step is to mass average the flow variables so each iteration is performed over the circumferential sections. In this way, radial profiles over the corresponding flow variables can be obtained. The profiles from one side to the other side of the interface are then exchanged and applied as a boundary condition. In this way, the averaged flow variables at the mixing plane will be equal and thus satisfy conservation of mass, momentum and energy [21]. Denton [22] pointed out that additional entropy was generated due to shock waves and artificial losses due to numerical errors. This extra loss will exceed the loss generated in the actual mixing process, which occurs at multi-stage interfaces [21]. For transonic compressors, it is therefore reasonable to conclude the mixing-plane method lead to under-prediction of the actual polytropic efficiency.

### 3.3.2 Computational Domain

The computational domain has been constructed using a general structured non-orthogonal multi-block mesh generator called G3dmesh. O-grids are used for resolution around the blade profile, while h-grids are used for the blade passages. The use of wall functions require  $y^+$  values in the region 20 – 100. The computational grid consist of 211000 cells, with approximately 100000 cells per domain. The design grid used for computation is illustrated in Fig 3.10.

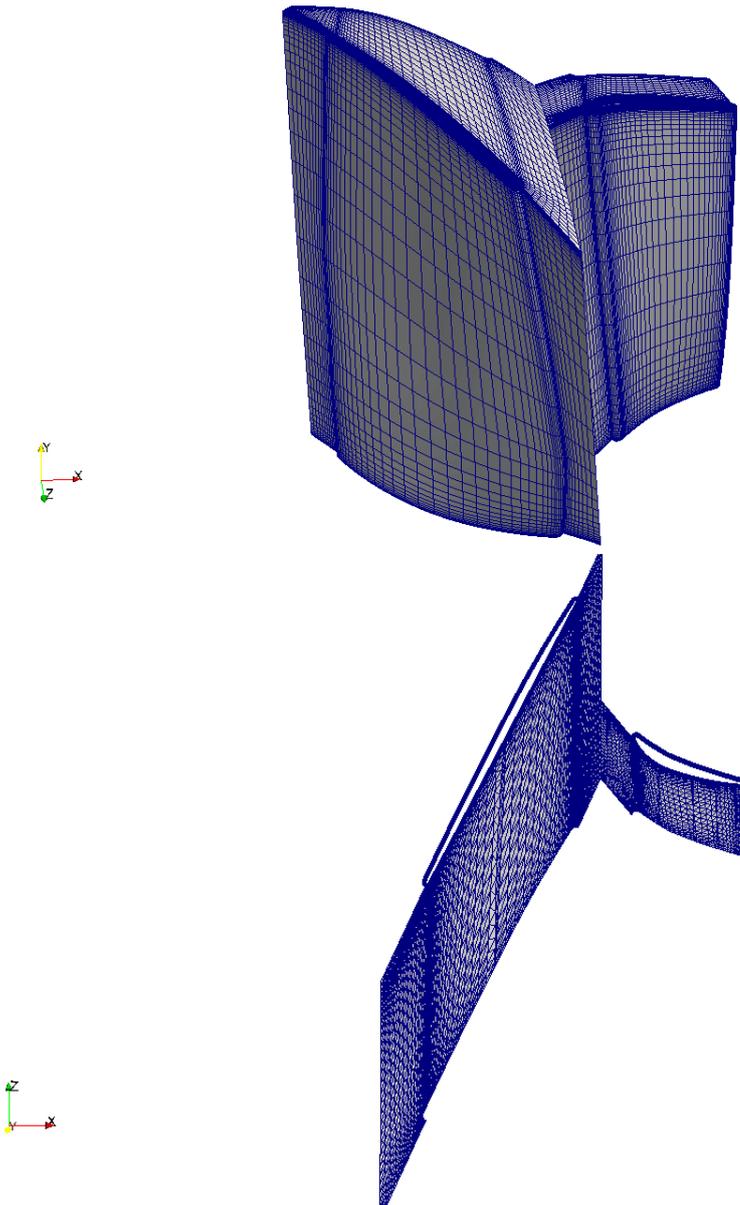


**Figure 3.10:** *3D grid surfaces and Blade-to-blade plane for rotor stator configuration*

### 3.3.3 Settings

#### 3.3.3.1 Mesh Settings

The 3D grid is generated by defining how many cells that should be included in each direction. These cells are given a direction in 3D space with corresponding number of nodes for each block number. A command file for rotor and stator is created where the input parameters for the grid are defined. The blade geometry in the command file is represented as an SNC profile. Hub, mid, shroud and tip from the command file is defined as SOR surfaces. The command file is then exported to a module translating the input from the command file, generating a 3D grid around the blade profile. Stretching are taken care of by patching blocks at inlet, outlet and passages. The module is generating an output file containing the grid properties, which is then exported to G3dmesh for meshing.

#### 3.3.3.2 Solver Settings

In order to start the CFD simulation, the necessary inputs required are included in the run file. Solver settings, including numerics and flow properties required to start the simulation are listed below

- Specify blade row speed
- Specify number of blades
- Specify rotation angles for rotor and stator
- Specify number of time steps
- Specify convergence criteria
- Specify CFL number
- Specify turbulence model
- Specify model constants and realizability factor for turbulence model
- Specify gas properties
- Specify extra damping for pressure and density

#### 3.3.3.3 Generate Mesh and Run CFD

When the set up is done and the mesh is generated, the case is set to run. The solution is initialized using a previous solution. The flow variables in each cell are linearly interpolated between the inlet and outlet boundaries. Convergence are monitored by checking mass averaged total- temperature and pressure as well as inlet- and outlet mass fluxes.

# 4

## Results

In this chapter, results from the optimization and CFD simulations are presented and discussed.

### 4.1 Optimization

The optimization is based on the procedure described in section 3.2, where the inlet and outlet radius for each span, together with the axial distance between the radius was kept constant.

From the individual blade element optimization, where stacking is not considered, the optimal variable ranges could be found. The final iteration of the individual optimization is shown in Fig 4.1 for hub, mid and tip span. The individual blade elements are found to be a good match of the reference blade. The variable values found from this optimization were used as range for the complete blade optimization, where the stacking of blade elements will be considered. The thickness values were calculated from the preliminary camber line described in section 3.2.5 and kept constant to save time.

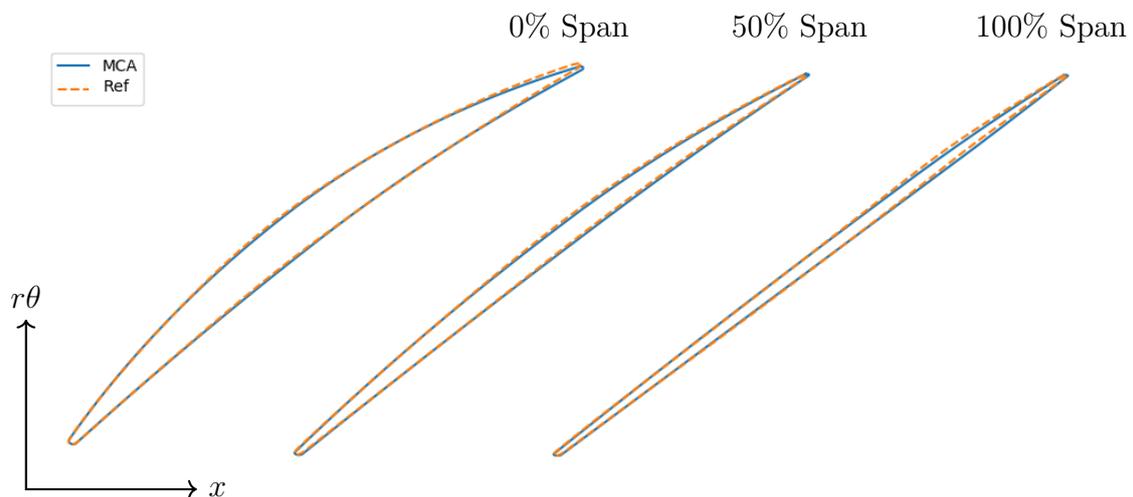


**Figure 4.1:** Comparison of MCA and reference blade elements at hub, mid and tip illustrated in  $r\theta$  plane for the individual optimization

The Pareto front from the final iteration of the complete blade optimization is illustrated in Fig 4.2. It shows a trade off between blade shape fit and blade stacking has to be made. It also shows that it is difficult to get a low deviation in the stacking. The stacking deviation determines axial sweep of the blade. Therefore, it was deemed that the blade shape will have a larger impact than the stacking, and a design with low average distance in  $r\theta$  was chosen.

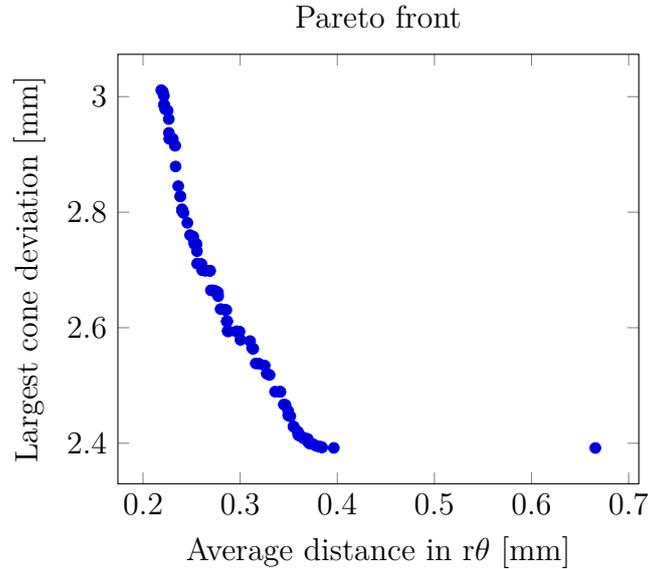


**Figure 4.2:** *Pareto front from the final iteration*

The selected MCA blade design is compared with the reference blade, which is illustrated in Fig 4.3 at hub, mid and tip.

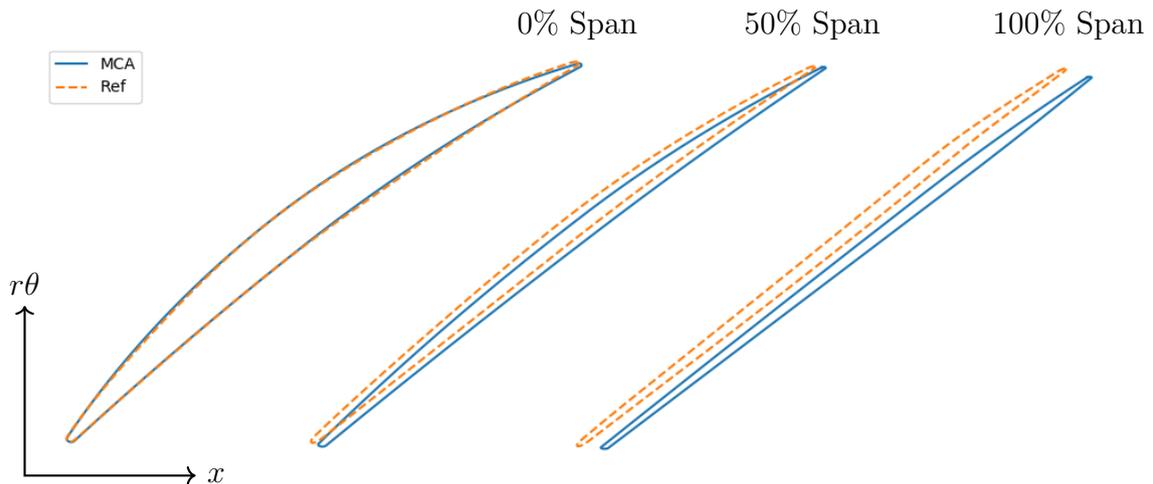


**Figure 4.3:** *Selected MCA design and reference blade at hub, mid and tip from the pareto front illustrated in the  $r\theta$  plane*

The blade comparison shows that for the MCA blade, stacking deviates increasingly along the span while the general blade shape at each span corresponds well with the reference blade.

## 4.2 CFD

### 4.2.1 Stage Performance

To evaluate the stage performance, the MCA and reference blade are compared in the same stage where the stator blade is same for both cases. The speedline for full rotational speed is constructed. The speedline was obtained from operating points generated with CFD simulations at varying pressure ratios. From the operating line, the design point, DP, was obtained by finding the intersection between the operating line and speedline. The design point from the MCA and reference blade is presented in Fig 4.4.

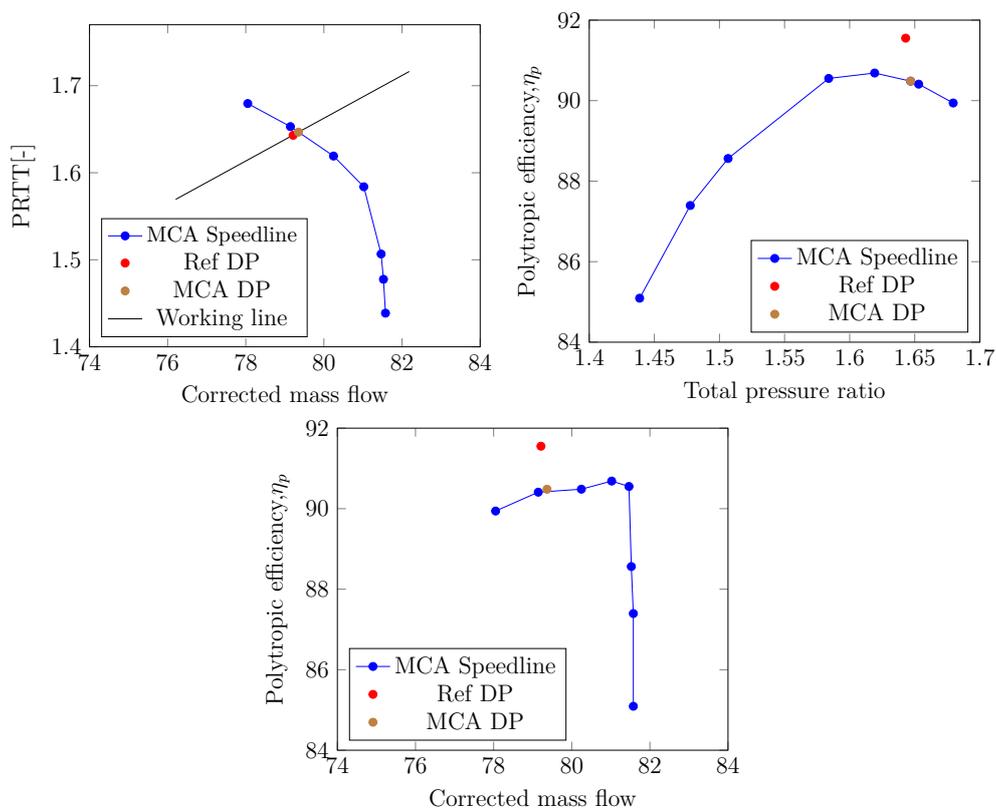


**Figure 4.4:** *Compressor performance of MCA and reference blade at design speed*

By assuming constant polytropic efficiency, an arbitrary operating point on the working line defined by the throttle area was obtained by varying the pressure ratio, and thereby calculating the corresponding mass flow. In this way, a large number of operating points could be obtained and a working line could be constructed. Once the working line is obtained, the distance between the two design points at design speed can be evaluated. At design speed it can be seen from Fig 4.4 that the reference blade produces higher polytropic efficiency compared to the MCA blade. Peak stage efficiency of the reference blade is roughly 1% higher compared to the MCA blade. Performance of the individual components in the stage for the two blades are outlined in table 4.1

## 4. Results

---

Properties	MCA blade	Ref blade	Notation
Inlet mass flow [ $\frac{kg}{s}$ ]	38.595840	38.520980	$\dot{m}_1$
Outlet mass flow [ $\frac{kg}{s}$ ]	-38.596910	-38.52222	$\dot{m}_2$
Mass flow difference [%]	0.2772	0.3219	$(\frac{\dot{m}_1 - \dot{m}_2}{\dot{m}_1}) * 100$
Total pressure ratio [-]	1.646802	1.642992	$PRTT$
Corrected mass flow [ $\frac{kg}{s}$ ]	79.366195	79.211890	$\dot{m}c_{orr}$
Polytropic efficiency [%]	90.4839	91.5516	$\eta_p$
Static pressure coefficient, rotor [-]	0.412576	0.424000	$C_{pR}$
Static pressure coefficient, stator [-]	0.181741	0.169914	$C_{pS}$
Static pressure coefficient, stage [-]	0.348638	0.355734	$C_{pRS}$
Pressure loss coefficient, rotor [-]	0.066837	0.057608	$\omega_R$
Pressure loss coefficient, stator [-]	0.043688	0.042623	$\omega_S$
Mean Swirl out [ $^\circ$ ]	-10.050894	-10.189522	$\bar{\alpha}_2$
Mean Swirl in [ $^\circ$ ]	-16.770996	-16.902688	$\bar{\alpha}_1$

**Table 4.1:** *Performance for optimized and reference blade at design speed*

The results summarized in 4.1 conclude that the performance agree fairly well. Although the blades perform almost identical in terms of corrected mass flow and total pressure ratio, a difference in polytropic efficiency can be noticed. Pressure loss coefficient for stator and rotor is shown to be higher in the MCA blade compared to the reference blade. An attempt to give more qualitative analysis to why there is a discrepancy in efficiency is provided in the following sections.

## 4.2.2 Simulation Results

The radial distribution of static pressure and Mach number magnitude are shown at approximately 80% and 95% span in the form of contour plots, highlighting the main differences between the two blades.

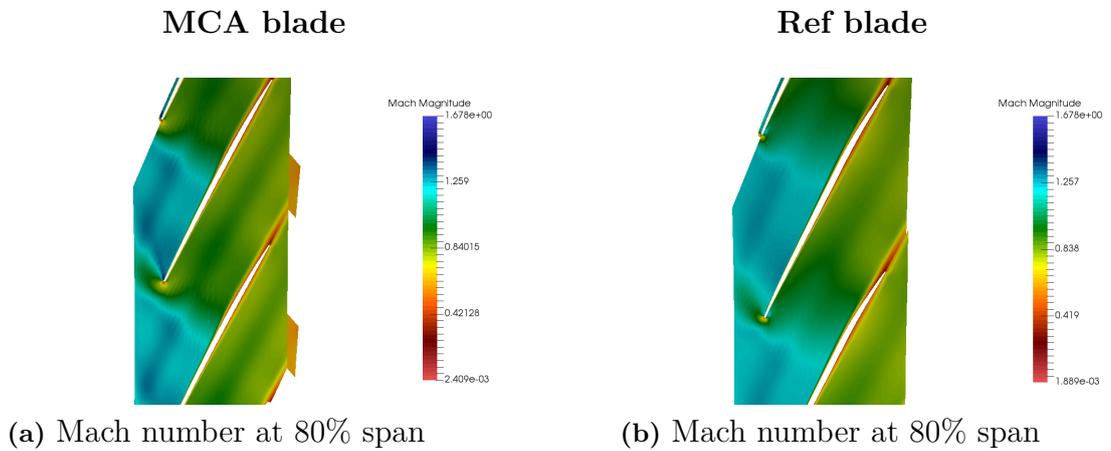


**Figure 4.5:** Cascade comparison of Mach number for the blades at 80% span

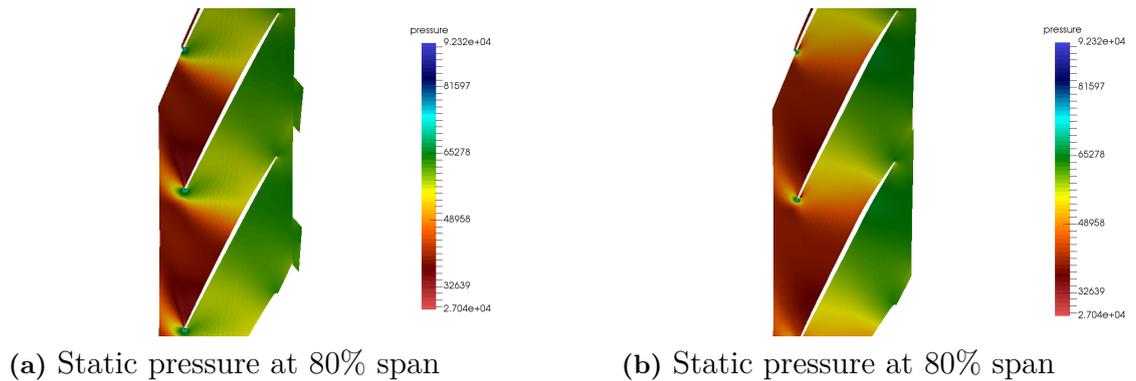


**Figure 4.6:** Cascade comparison of static pressure for the blades at 80% span

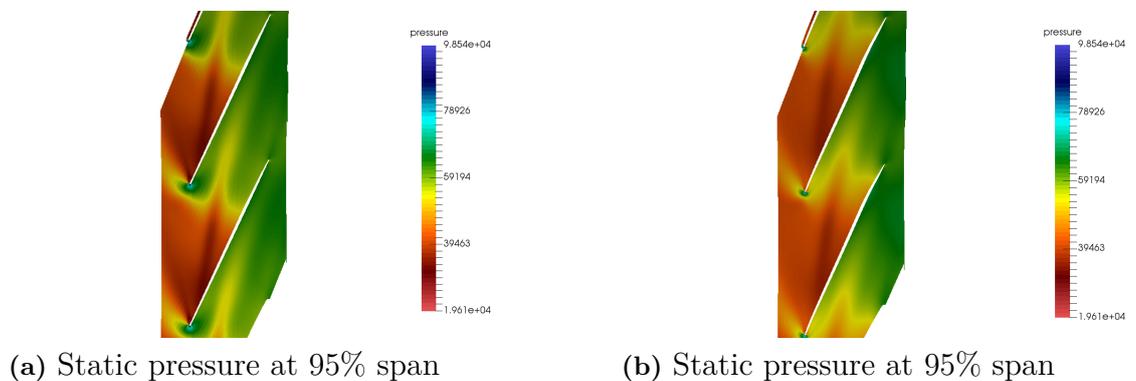


**Figure 4.7:** Cascade comparison of static pressure for the blades at 95% span

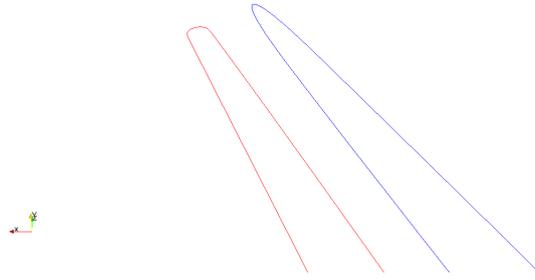


**Figure 4.8:** *Comparison of leading edge thickness for the two blade profiles*

Illustrated in Fig 4.5 and 4.6, a detached shock is formed at the blade leading edge. The MCA blade has a slightly higher incidence at the tip compared to the reference blade. This implies that a suction peak is formed near the leading edge, whereby the flow is decelerating. Shown in Fig 4.5a the Mach number at the suction surface is slightly higher compared to the reference blade, which may be due to slightly more curvature at the MCA blade, contributing to an acceleration of the flow due to an increase in Prandtl-Meyer turning. The higher Mach number downstream produces a near normal passage shock, terminating at the neighbouring blade suction surface. From Fig 4.6, the passage shock is more normal compared to the reference blade which is slightly more oblique, leading to an increase in shock strength and entropy and hence shock losses and loss in total pressure. The increase in intensity of the passage shock for the MCA blade may lead to an increase in shock-vortex interaction as the tip-vortex crosses the shock. The shock-vortex interaction leads to a deceleration of the flow, resulting in a sudden expansion of the flow and ultimately to vortex breakdown. From Fig 4.5 and 4.6, the stronger passage shock from the MCA blade leads to a larger static pressure gradient compared to the reference blade. Shock losses in combination with mixed out losses from tip vortex breakdown contribute to total pressure loss and thus an increase in entropy, resulting in a reduction in aerodynamical performance, and hence lower the efficiency of the compressor. This may be an explanation to why there is a discrepancy in efficiency between the two blades.

#### 4.2.2.1 Spanwise distribution of total pressure and swirl

The spanwise profiles of total pressure and swirl at rotor leading and trailing edge as well as stator trailing edge are presented in Fig 4.9 and Fig 4.10.

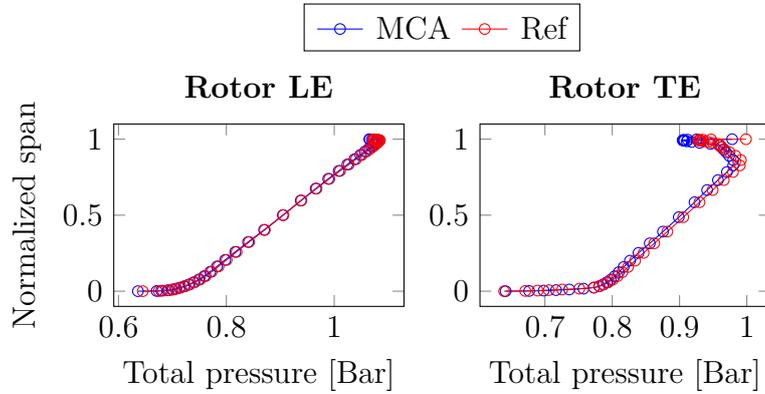


**Figure 4.9:** *Normalized radial span distribution of total pressure before and after rotor*

Overall, the results for the two blade profiles agree very well except for a small deviation in total pressure at the trailing edge. The MCA blade is shown to produce a loss in total pressure close to the shroud, this may be due the change in geometry from the optimization, where the MCA blade was shown to have a thicker leading edge compared to the reference blade, as well as more curvature on the suction surface, leading to a stronger passage shock and hence an increase in shock loss and shock-vortex interaction. The same spanwise profiles for the rotor are plotted for the stator in Fig 4.10. Note that the same stator design is used for both stages and the legend MCA and reference denotes the stage.

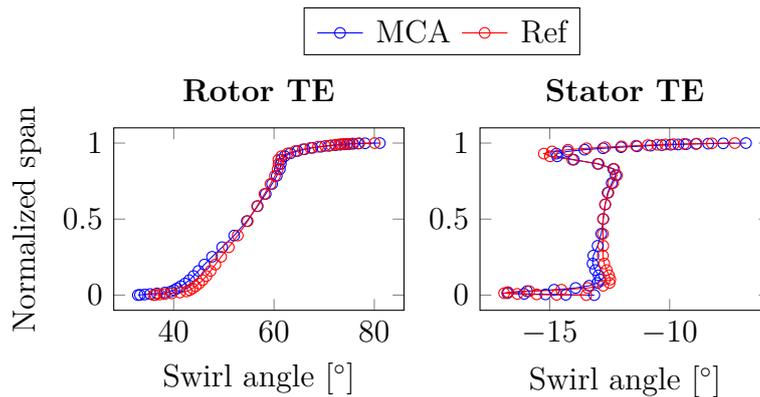


**Figure 4.10:** *Normalized radial span distribution of swirl angle after the rotor and stator*

Illustrated in Fig 4.10, swirl increases in the rotor and is added to the flow, and according to the Euler work equation, an increase in total energy is produced by a change in angular momentum. The task of the stator is to remove the swirl from the flow, implying that the stator cannot add energy to the flow, but instead converting

## 4. Results

---

kinetic energy of the flow into internal energy by raising the static pressure. Fig 4.10 show that the the swirl for the two blade profiles are well matched for both stator and rotor trailing edge.

# 5

## Conclusion

A multi-objective optimization of transonic compressor MCA blades has been accomplished with the use of NSGA-II as the genetic algorithm. Computational fluid dynamics has been used as a tool to compare the performance of the MCA blade with the reference blade. In order to recreate the reference blade with MCA geometry, two objective functions were formulated. The first objective describe the mean average deviation in the  $r\theta$ -plane, and the second objective describes the cone displacement in the axial direction, ensuring that the blade elements are correctly stacked. These objectives were optimized using five design variables at 15 spans, describing the MCA blade geometry, resulting in a total of 75 optimizing variables. NSGA-II produces a Pareto-optimal front of the conflicting objectives, producing compromised solutions which enhances the result. Results from the optimization showed an increase in leading edge thickness of the MCA blade compared to the reference blade, which may contribute to an increase in shock loss. This may be resolved by describe the leading edge in the form of an ellipse or higher order polynomial instead of a circle. This would likely yield a more oblique leading edge, which would be beneficial as it would reduce the shock strength. From CFD it was shown that the reduced order model is capable of predicting the overall compressor characteristics in terms of total to pressure ratio and corrected mass flow. However, the reference blade produce a slightly higher polytropic efficiency compared to the MCA blade. It was found that the difference between corrected mass flow and total pressure ratio was  $\approx 0.2\%$ . Sequential quadratic programming was also used as an optimizing method too see if it is feasible to reduce the computational cost. It was shown that the SQP was significantly faster optimizing one individual blade span. By comparison, it took 15 minutes to optimize one span using the NSGA-II, while it took  $\approx 15$  seconds with the SQP. A grid independence study was not carried out due to time limitations, this would have been beneficial as it would provide a finer mesh with retained accuracy. The conclusion is that the model is capable of recreating an already optimized blade with MCA blade geometry and producing results similar to those of higher order models. Hopefully, these results could pave the way for new loss correlation models.

### 5.1 Future Work

It would be interesting to see if mean geometric deviation could be reduced further, as the mean geometrical deviation resulted in a more blunt leading edge compared to the reference blade, this could have contributed to a decrease in efficiency of the compressor. It would also be interested if the CPU time for optimization could be reduced as the computational cost is very high due to the vast amount of optimizing variables. In hindsight, the optimization can be reduced to a single-objective problem by remove the second objective and instead use 3D interpolation between the two blade profiles. This could be included in future work. Other optimizing methods such as radial basis functions and metamodels in combination with NSGA-II could be implemented in order to reduce the computational cost. Sequential quadratic programming (SQP) would also be an interesting alternative for optimization. In order to do more thoroughly analysis of the flow field, other turbulence models could be tested.

# Bibliography

- [1] Saravanamuttoo, H.H., Rogers, G.F.C., Cohen, H., Straznicki, P.V.(2009). Gas turbine theory. 6th edition. Pearson Education Limited. ISBN:978-0-13-222437-6
- [2] Crouse, James E., Janetzke, David C., Schwirian, Richard E. A computer program for composing compressor blading from simulated circular-arc elements on conical surfaces, NASA, 1969.
- [3] Dixon, S. L. and C. A. Hall.2014. Fluid Mechanics and Thermodynamics of Turbomachinery. 7th ed. Butterworth-Heinemann. ISBN:978-0-12-415954-9
- [4] Anderson, John.(2003).Modern compressible flow with historical perspective. 3rd edition. New York: McGraw-Hill. ISBN:978-0-07-242443-0
- [5] Biollo, R., Benino, Ernesto.2012. Recent advances in transonic axial compressor aerodynamics. *Progress in aerospace sciences*. 56 (2013), 1-18.
- [6] Cumpsty, N.A. 2004. Compressor Aerodynamics Krieger Publishing Company, Malabar,Florida. ISBN:1-57524-247-8
- [7] Ellbrant, L.2014. Multi-objective CFD-based design method for axial compressors. PhD-thesis., Gothenburg: Chalmers University of technology. ISBN: 978-91-7597-069-1
- [8] Davidson, L. 2003. An Introduction to Turbulence Models Gothenburg: Chalmers university of technology.
- [9] Andersson, B., Andersson, R., Håkansson, L., Mortensen, M., Sudiyo, R., Wachem, B. 2017. Computational Fluid Dynamics For Engineers. 13th edition. Cambridge University press.
- [10] Deb, K., Pratap, A., Agarwal, S., and Meyarivan, T., 2000. A fast and Elitist Multi-Objective Genetic Algorithm: NSGA-II. KanGAL Report 200001, Indian Institute of Technology Kanpur, Kanpur, PIN 208016, India.
- [11] Andersson, N.2005.A Study of Subsonic Turbulent Jets and their Radiated Sound Using Large-Eddy Simulation. PhD thesis, Chalmers University of Technology, Gothenburg. ISBN: 91-7291-679-6
- [12] Greitzer,E.M.1980.REVIEW-Axial Compressor Stall Phenomena. *Journal of Fluids Engineering*,102(2).134-151.
- [13] Lieblein, S., Schwenk, F.C., Broderick, R.L. 1953. Diffusion factor for estimating losses and limiting blade loadings in axial-flow-compressor blade elements. NACA R.M. E53 D01.

- [14] Denton, J. D. 1993. Loss mechanisms in turbomachines. IGTI scholar lecture. *ASME Journal of Turbomachinery*, 115, 621-656.
- [15] Schobeiri, M.T. 1997. Advanced Compressor Loss Correlations. *International Journal of Rotating Machinery*, Vol.3, 163-177.
- [16] Jingjun, Zhon., Shaobing, Han., Huawei, Lu., Xiaoxu, Kan. (2013). Effect of tip geometry and tip clearance on aerodynamic performance of a linear compressor cascade. *Chinese Journal of Aeronautics*, 26(3), 583-593.
- [17] S, Sakulkaew., C.S, Tan., E, Donahoo., C, Cornelius., M, Montgomery.2013. Compressor Efficiency Variation With Rotor Tip Gap From Vanishing to Large Clearance. *ASME Journal of Turbomachinery*, 135(3), 1-10.
- [18] Carter, A.D.S. 1950. Low-speed performance of related aerofoils in cascade. ARC. Current Paper, No.29.
- [19] Howell, A.R.1945. Fluid dynamics of axial compressors. *Proceedings of the Institution of Mechanical Engineers*, 153.
- [20] Lakshminarayana, Budgur.1996. Fluid Dynamics and Heat Transfer of Turbo-machinery. New York: Wiley. ISBN:0-471-85546-4
- [21] Culver, R., Liu, F. and Montgomery, M. 2009. Computational Study of Asynchronous Vibrations in a 1.5 Stage Transonic Compressor. *45th AIAA/ASME/SAE/ASEE Joint Propulsion Conference and Exhibit*.
- [22] Denton, J.D.1992. The Calculation of Three-Dimensional Viscous Flow Through Multistage Turbomachines. *Transactions of the ASME*, Vol 114, 18-26.
- [23] Råde, L., Westergren, B. 1999. Mathematics Handbook for science and Engineering. 4th edition. New York, Springer-Verlag Berlin Heidelberg. p.166, eq 249.

# A

## Appendix 1